Fast machine learned α-Fe-H interatomic potential for hydrogen embrittlement

Eetu Makkonen* and Flyura Djurabekova Department of Physics, University of Helsinki, Finland

Alvaro Lopez-Cazalilla
Barcelona Supercomputing Center, Plaça Eusebi Güell 1-3, 08034 Barcelona, Spain
(Dated: November 27, 2025)

In this work, we present a machine-learned interatomic potential for the α-Fe-H system based on the tabulated Gaussian Approximation Potential (tabGAP) formalism. Trained on a Density Functional Theory (DFT) dataset of atomic configurations, energies, forces, and virials, the potential is designed to address the issue of H-induced acceleration of mechanical failure of metals, generally known as hydrogen embrittlement (HE). The proposed potential is shown to outperform the widely used classical and machine-learned interatomic potentials in fundamental properties of the α-Fe-H system. We show that the tabGAP model reproduces H-point defect properties, Hdislocation interaction, H-H interaction, and elastic constants with nearly DFT-level accuracy at a computational cost that is competitive with the efficient classical Embedded Atom Method (EAM) potentials. We further demonstrate the utility of the tabGAP model in molecular dynamics simulations of tensile tests of a perfect, and a (111)[112]-notched α -Fe structure with and without the load of H atoms. The simulations show evidence of HE via observation of accelerated decohesion of Fe atoms at the tip of the notch, and an increase in vacancy concentration driven by H-dislocation interactions. Hence, the results of the presented simulations support the hypotheses of hydrogenenhanced decohesion (HEDE) alongside hydrogen-enhanced strain induced vacancies (HESIV) as important mechanisms for H-induced mechanical failure of iron systems.

I. INTRODUCTION

Hydrogen embrittlement (HE) is the phenomenon of H-induced increase of mechanical failure probability in various metals such as nickel, iron, and different steels. It is one of the long-standing problems in material science due to its high complexity, arising from processes spanning multiple spatial and temporal scales. Although the effect of HE is mainly observed as premature failure in structural metals at the macroscopic scale, the currently accepted HE mechanisms are triggered at the nanoscale, involving various interactions of hydrogen atoms with different microstructural imperfections. These include vacancies and their complexes, dislocations, grain boundaries, and crack tips [1, 2]. Gradually, it has become clear that HE is not driven by a single type of H-defect interaction but rather the result of multiple processes that play key roles in driving the material toward premature mechanical failure [1]. Understanding these nanoscale phenomena and their emergent outcomes requires spatial and temporal resolutions that are currently inaccessible even by the most advanced experimental methods. Hence, if a high-accuracy description of interatomic interactions is available, computational modeling can become an irreplaceable technique in increasing the understanding of H effects in metals to enable the development of H-based green energy applications.

Various computational studies have addressed HE in iron and steels using the molecular dynamics (MD)

method [3–7]. The known roadblock in these simulations is the large size difference between the metal and H atoms. This gives rise to considerable differences in the characteristic time and length scales of the two species, where the light H atoms might move unacceptably far during a single timestep, leading to numerical errors and invalidating the simulation result. In addition, the details on kinetic paths of the light H atoms are lost. Due to this, the satisfactory capture of H-related kinetics requires reduction of the simulation timestep. To enable simulations at relevantly long timescales along with a reduced timestep, a computationally efficient interatomic potential (IAP) is needed.

MD simulations of HE effects have typically used simple and computationally efficient IAPs based on the classical embedded-atom method (EAM) [5–8]. Although very fast, classical IAPs suffer from poor accuracy outside the interactions and material properties to which they were specifically fitted. This is partially attributable to their fixed functional forms. Thus, machinelearning IAPs (ML-IAPs) have become increasingly popular because of significant improvements in the areas of interatomic interactions where classical potentials usually fail [9, 10]. The flexible functional forms of ML-IAPs have proved to be capable of reproducing the properties of multiple different types of defects present in metallic solids in addition to the exclusive description of bulk mechanical properties. This holds also for concentrated alloys with high chemical complexity [11– 13

Although superior in the description of material properties, ML-IAPs generally suffer from the main drawback of a fairly high computational cost compared

^{*} Contact author: eetu.makkonen@helsinki.fi

to that of classical IAPs. Although the performance efficiency of individual IAPs varies drastically, in general, the efficiency of classical IAPs is evaluated to be in the order of 1×10^{-3} milliseconds/(atom × step), while the performance of many equally or more accurate ML-IAPs is evaluated above 1×10^{-1} milliseconds/(atom × step), 100 times slower [11, 14].

In this work, we propose an efficient ML-IAP based on the tabulated Gaussian approximation IAP (tabGAP) formalism [11, 12, 15, 16] for the α -Fe-H system. In this potential, we focus only on the body-centered cubic (bcc) phase of Fe, which forms the backbone of low-carbon steels, the main materials of interest in HE research. We verify the properties of the H-loaded Fe crystal lattice given by our tabGAP against DFT results, and the classical and ML-based potentials available in the literature for the same system. Furthermore, we use our tabGAP in MD tensile test simulations of a perfect, and a notched, α -Fe structure with and without H atoms with the goal of elucidating possible HE mechanisms.

II. METHODOLOGY

A. Gaussian approximation potentials

The developed potential presented in this work is based on the Gaussian approximation potential (GAP) framework first introduced by Bartok et al. [15, 16]. We defined the developed Fe-H GAP as a combination of three low-dimensional descriptors, namely a two-body (2b), a three-body (3b), and an EAM descriptor. This combination has previously been shown to provide an incredible combination of low computational cost (after tabulation; see section IIC), and flexibility in metallic systems [11, 12]. In addition, a fixed analytical Coulomb potential is added to reproduce short-range repulsive interactions between species [17]. This way, the non-short-range interactions are left to be machine-learned. Accordingly, the total energy expression for the GAP is defined as

$$E_{tot} = E_{rep.} + \sum_{d} \delta_d^2 \sum_{i}^{N} \sum_{s}^{M_d} \alpha_s K_{se}(\boldsymbol{q}_{d,i}, \boldsymbol{q}_{d,s}) \qquad (1)$$

where the sum over $d \in \{2b, 3b, EAM\}$ denotes the sum over the descriptor set. The contribution of each descriptor is calculated by summing N target atomic environments i and M_d sparse reference environments s. In addition, the descriptor contributions are scaled by the hyperparameter δ_d^2 . The variables α_s are the regression coefficients obtained from independent Gaussian process regressions. We use the squared exponential kernel (K_{se}) for measuring the similarity of the target $(q_{d,i})$ and reference $(q_{d,s})$ configurations.

Furthermore, the repulsive energy term $E_{rep.}$ in Eq. 1

has the Ziegler-Biersack-Littmark (ZBL) potential form

$$E_{rep.} = \sum_{i < j}^{N} f_{cut}(r_{ij}) \phi(\frac{r_{ij}}{a}) \frac{1}{4\pi\varepsilon_0} \frac{Z_i Z_j e^2}{r_{ij}}, \qquad (2)$$

where a is defined as

$$a = \frac{0.46848}{Z_i^{0.23} + Z_i^{0.23}}. (3)$$

The difference between the Eq. 2 and the universal ZBL potential [18] is that the screening function $\phi(\frac{r_{ij}}{a})$ is fit to repulsive Fe-Fe, Fe-H, and H-H dimer data computed with all-electron DFT [19]. The repulsive contribution by this energy term is restrained by the smooth cutoff function $f_{cut}(r_{ij})$, which was set to 0.4–0.6 Å for H-H, 1.0–1.3 Å for Fe-H, and 1.8–2.2 Å for Fe-Fe interactions.

1. Hyperparameter optimization

The definitions of the descriptors within the GAP framework contain several hyperparameters that can be tuned to maximize performance of the fitted IAP [20]. In Tab. I we summarize the most notable hyperparameters used for the training of the Fe-H tabGAP presented in this work. During the training procedure we noticed that using different energy scales (δ_d) according to the pertaining species led to a remarkable improvement in the performance of the potential. Since the scales of the energy surfaces for the Fe-Fe interactions and for the H-H interactions differ substantially, this double hyperparameter has a physical justification. In other words, we set the δ parameter for the 2b-FeFe and 2b-FeH descriptors to be 10.0, while δ for the 2b-HH descriptor was set to 5.0. Similarly, δ for any 3b-descriptor modeling H-H interactions was set to 0.1, while δ for the other triplets was set to 1.0. Separating the δ -parameters for the EAM-descriptors showed no improvement, and, hence, we left them to be the same for both species.

For the energy, force, and virial regularization parameters σ , we followed the scheme in Ref. [11] for pure Fe structures, with default values set to 1 meV, $10\,\mathrm{meV/\mathring{A}}$, and $100\,\mathrm{meV/\mathring{A}}^3$, respectively. For Fe-H structures, we used a stronger regularization of 2σ for structures with higher local H concentration, such as vacancy-H structures with > 6 H atoms near the vacancy. Structures with a single H atom in the O-site, T-site, or the T-T transition saddle point used a weaker regularization of 0.5σ . The free H-trimer configurations used a stronger regularization of 10σ . These are more detailedly explained in the Supplemental Material.

B. Training and testing dataset

The dataset for the present Fe-H tabGAP is extended from the previously published tabGAP for the pure α -Fe [11]. In the present work, the extended dataset

TABLE I: Hyperparameters used for the descriptors in training a GAP model for α -Fe-H: cutoff radius $r_{\rm cut}$, width of the cutoff region $r_{\Delta {\rm cut}}$, energy scale δ , and the number of sparse descriptor environments M. For clarity, shared hyperparameters between descriptors of the same type are not repeated.

Descriptor	$m{r}_{\mathrm{cut}} \; (\mathrm{\AA})$	$r_{\Delta \mathrm{cut}} \ (\mathrm{\AA})$	δ	M					
EAM									
Fe H	4.5	1.0	1.0	30					
	Two-	body							
FeFe FeH HH	4.5	1.0	10.0 10.0 5.0	20					
	Three	-body							
FeFeFe FeFeH HFeFe FeHH HFeH HHH	3.7	0.6	1.0 1.0 1.0 0.1 0.1 0.1	800					

includes various configurations of isolated H, and α -Fe-H structures calculated by means of Density Functional Theory (DFT), using the Vienna Ab initio Simulation Package (VASP), the version 5.4.4 [21–24]. The electronic structure calculations were used in deriving the total energies, atomic forces, and virials for the training and testing datasets. These are the target properties of the Gaussian process regression.

Since the accuracy of the DFT calculations also rely on the selection of several critical input parameters, for consistency of the dataset extension, in this work we used the same parameters adopted by Byggmästar et al. [11], since the pure α -Fe training data were inherited from their work. Maintaining consistent DFT parameters ensures coherency within the dataset, which is important when using ML methods.

The exchange-correlation (XC) functional employed was the Perdew–Burke–Ernzerhof (PBE) generalized gradient approximation (GGA) [25]. The projector-augmented wave (PAW) pseudopotential was employed, with the 16 valence electron variant selected for Fe [26]. For H, the standard PAW pseudopotential with one valence electron was used. Additionally, aspherical contributions inside the PAW spheres were included. The plane-wave energy cutoff was set to 500 eV.

The Brillouin zone integration employed a k-point grid spacing of 0.15 Å $^{-1}$. The self-consistent field convergence criterion was set at $1\times 10^{-6}\,\mathrm{eV}$. All calculations were performed with collinear spin polarization, which yields the ferromagnetic state of $\alpha\text{-Fe}$. The Methfessel–Paxton first-order smearing method was employed with a smearing width of 0.1 eV.

The Fe-H structures in this work were mainly generated with two methods: by randomly displacing atoms in ideal initial structures obtained from DFT relaxation, and by sampling frames from finite-temperature (200–400 K) MD simulations using an earlier tabGAP version. The first method was used in the beginning of the tabGAP model development, and the second method was used later once the model became usable.

The main contents of the final dataset is covered by the following structure classes:

- bcc Fe lattices with interstitial solute H atoms
 - -2-20 at.% H content
- Distorted bcc Fe lattices with interstitial H
 - Both uniaxial, and fully random cell distortions
 - Strains in the range of -10-10%
 - -2 and 10 at.% H content
- \bullet Fe vacancy -H structures
 - 1 to 14 H atoms near or inside the vacancy
- Short-range H-H and H-H-H configurations
 - H-atoms in neighboring T-sites ($d_{H-H} \approx 1.6-3 \,\text{Å}$)
 - H-atoms near the same T-site $(d_{H-H} \approx 0.5-1.6 \text{ Å})$
- Fe self-interstitial atoms with one or three nearby H atoms
- H-atoms in the O-site
- H in the T-T migration path saddle point
- Free H-dimer and H-trimer configurations

The content of the structure dataset reflects the main focus of the presented potential: the accurate capture of free H interaction, and both H-Fe and H-H interaction in bulk α -Fe. Due to the stark difference in the chemical behavior of H in these two environments, this is not an easy fitting problem for low-dimensional IAPs. It is known from DFT calculations that when H is placed inside a metal lattice like α -Fe , it mostly loses its ability to form covalent bonds with other H atoms, and instead dissociates to distances $d_{H-H}{>}1.9\,\text{Å}$ [3], compared to its free H-H bond length of \sim 0.74 Å. Care was taken to ensure that the dataset covered this difference in H-H interaction via introducing α -Fe-H lattices with d_{H-H} down to 0.5 Å.

C. The tabGAP formalism

To reduce the high computational cost of the developed GAP model [14, 17], the tabGAP method introduced by Byggmästar et al. [27] was used, in which the two-body and three-body energy contributions from the selected low-dimensional descriptors are tabulated onto their respective one-dimensional and three-dimensional grids. After tabulation, energies can be efficiently and accurately evaluated with spline interpolation between

the grid points. Given a sufficiently dense grid, the interpolation error becomes inconsequential, while the computational cost is reduced by approximately two orders of magnitude. This makes the tabGAP model competitive with the cost-efficient classical EAM potentials while maintaining a nearly quantum-mechanical level of accuracy [27]. For the Fe-H tabGAP, the interpolation grids of 5000 and $120 \times 120 \times 120$ were adopted for the 2b and 3b descriptors, respectively.

D. Molecular statics and dynamics

For all molecular static (MS) and molecular dynamics (MD) simulations, we used the open-source software LAMMPS [28]. In MS calculations, the energy and pressure of the structures were minimized with the Polak-Ribiere conjugate gradient (CG) algorithm. The H migration pathways were calculated with the climbing image nudged elastic band method (CI-NEB) with 13 replicas, and a spring constant of $1.0\,\mathrm{eV/\AA}$ for the nudging forces [29]. All MD simulations were performed at 300 K in either the NVT or the NPT thermodynamic ensemble, starting with a structure pre-relaxed with CG.

For the LAMMPS-implementation of the tabGAP formalism, see Ref. [30].

III. RESULTS

A. Training and testing errors

II reports the energy and force root-meansquare errors (RMSEs) for the Fe-H GAP and tabGAP potentials calculated for training and testing sets of structures relevant to the intended use of the potential. In general, both the energy and force errors are low, only a few meV/atom and $\sim 0.1 \,\mathrm{eV/A}$, respectively. The Hspecific force RMSEs are approximately double that of the total. A large fraction of this error originates from structures with unrealistically high local concentration of H atoms, for example, structures with a vacancy that contain 14 H atoms. If such structures are ignored in the error calculation, the force RMSE drops to $\sim 0.11 \,\mathrm{eV/A}$ for both training and testing sets with the tabulated potential. However, having such unrealistic structures in the training dataset of the Fe-H tabGAP was important for reproducing the physical behavior of H in the Fe lattice.

B. Computational efficiency

We evaluated the computational efficiency of the different IAPs by performing a 10000 time step NVT MD simulation for a $(6 \times 6 \times 6)$ α -Fe cell with three different interstitial H concentrations: 0.25 at.%, 1 at.%,

TABLE II: Root-mean-square errors (RMSE) for Fe–H GAP and tabGAP models on the training and testing sets. Energy errors (E_{total} , E_{FeH}) are reported in meV/atom and force errors (F_{total} , F_H) in eV/Å. E_{total} and F_{total} are computed over all structures, E_{FeH} is computed over structures that contain both Fe and H, and F_H is computed over all H atom forces.

	meV/	atom	eV/Å					
	$E_{ m total}$ $E_{ m FeH}$		$F_{ m total}$	$F_{ m H}$				
Training								
GAP tabGAP	2.20 2.23	1.18 1.29	$0.073 \\ 0.077$	0.135 0.154				
Testing								
GAP tabGAP	1.87 1.88	1.76 1.75	0.069 0.069	0.150 0.157				

and $10 \, \text{at.}\%$. The simulations were run on a single core of a Xeon Gold 6230 CPU.

The efficiency of the potentials is compared in terms of the computational time required to perform the simulation per atom and per time step. The comparison is presented in Tab. III in units of milliseconds/(atom × step). The lower this value, the more efficient is the used IAP. The presented Fe-H tabGAP appeared to be somewhat less efficient than the classical EAM IAPs (less than one order of magnitude difference), while its efficiency is two orders of magnitude higher than that of Meng_NNIP, which is another ML-IAP available in the literature. Computational efficiency is a complex function of many parameters, but it is roughly proportional to the average number of neighboring atoms per an atom. This is reflected in the table as a decrease in efficiency for all potentials when the concentration of H increases in the α -Fe lattice. The differences in scaling between the IAPs as a function of the H concentration are roughly explained by differences in descriptor cutoff distances, which resulted in slightly worse scaling of the Fe-H tabGAP as compared to the other IAPs.

C. Potential validation

1. H as a point defect in a-Fe

To validate the performance of the proposed potential, in Tab. IV we compare the most relevant characteristic energies that describe the presence of H atoms within the α -Fe lattice. These energies include; the solution energies for a H atom in a tetrahedral (T) and octahedral (O) interstitial sites, $E_{s,T}^H$ and $E_{s,O}^H$, respectively; the solution energy for a H atom within a vacancy $(E_{s,V}^H)$; the migration energy barriers from a direct transition between two tetrahedral sites $(E_{m,T-T}^H)$, or through an octahedral site between the two tetrahedral sites

TABLE III: The computational efficiency (milliseconds/(atom \times step)) of an MD simulations of a $(6 \times 6 \times 6)$ α -Fe structure at three different H concentrations. All simulations were run with a single CPU core.

H concentration (at.%)	tabGAP	Ram_EAM	Wen_EAM ^b	Kumar_EAM ^c	Meng_NNIP ^d
0.25	0.0096	0.0018	0.0017	0.0022	2.13
1.0	0.0105	0.0019	0.0019	0.0024	2.09
10.0	0.0172	0.0023	0.0023	0.0032	2.41
	a [31]	b [32]	^e [7] d [33]		

 $(E_{m,T-O-T}^H)$. Moreover, we include the energy values modulated by hydrostatic compressive/tensile strains $(\varepsilon = \pm 2\,\%)$ for the properties related to the more stable T-site.

We calculate the solution energies as

$$E_{s,X}^{H} = E(H_X) - E(X) - \frac{1}{2}E(H_2), \tag{4}$$

where $E(H_X)$ is the energy of a structure with a H atom in the X site, E(X) is the energy of the same structure excluding the H atom, and $E(H_2)$ is the energy of the free H₂ molecule. The migration energies were obtained using the CI-NEB method explained in Sec. II D. The results of these calculations are summarized in Tab.IV.

Of the two stable interstitial sites for H atoms in the α -Fe lattice (T- and O-sites), the T-site is known to be more stable for a H atom, with solution energy values ranging between 0.20–0.34 eV according to DFT estimates from the literature [3, 31, 34]. All IAPs listed in Tab. IV capture this property sufficiently well. Since the zero-point energy (ZPE), which has been shown to increase the solution energy of H [3], was not taken into account in either of the listed ML-IAPs, the solution energy in the present tabGAP and Meng_NNIP [33] are somewhat lower compared to the three classical EAM potentials.

The stability of the T-site persists also at moderate hydrostatic strains in the bcc lattice. In our calculations, we see that the solution energies at tensile and compressive strains of 2% are consistent with the non-ZPE corrected DFT estimates [31, 33]. All potentials report a directly proportional relationship between the solution energy of H and the density of the lattice, indicating that H would segregate to less dense regions of α -Fe.

Given the geometry of interstitial sites in a bcc lattice, a H atom has two main migration paths which it can take; the direct migration between two neighboring T-sites (T-T path, see Fig. 1a), or the path straight through an O-site between the T-sites (T-O-T path, see Fig. 1b). Both migration barriers are presented in Tab. IV where we observe that the Fe-H tabGAP is able to reproduce them satisfactorily. In particular, the T-O-T migration barrier is very close to that of the non-ZPE corrected DFT data [3], while the T-T barrier is $\sim 0.02\,\mathrm{eV}$ higher than commonly cited values. Nevertheless, this value is still within the experimentally observed range of $0.035-0.142\,\mathrm{eV}$ [35]. According to DFT calculations

[3, 35] both the T-T and T-O-T migration paths contain a single saddle point, the trend which is well reproduced by the Fe-H tabGAP. In addition, the T-T migration path is not straight but has a slight curvature toward the neighboring O-site. DFT calculations have predicted the distance between the saddle point of this T-T transition and the O-site to be 0.407 Å [35], and the Fe-H tabGAP predicts a very similar distance of 0.372 Å.

The migration paths of a H atom for the other IAPs are also reported in Fig. 1. The classical EAM IAPs, which are used in this study for comparison, are parameterized to include the ZPE-correction. As has been previously shown, the ZPE correction reduces the migration energy barrier for H diffusion in a metal lattice [3, 35]. Hence, both Ram_EAM and Wen_EAM successfully predict the lowered energy barriers. However, the calculation of the T-O-T type transition using the Wen_EAM IAP reports the O-site to be a metastable state and not a saddle point (see cyan curve in Fig. 1b), which contradicts the results of DFT calculations [35, 36]. The calculations of both the T-T and T-O-T transitions with the Kumar_EAM IAP resulted in complex energy curves with multiple saddle points, see the green curves in Fig. 1a and 1b. The other ML-IAP, Meng_NNIP, gave values close to those obtained with DFT and the tabGAP. For the detailed dependence of the migration energy barriers on hydrostatic strain, we guide the reader to the Supplementary Material.

2. H-vacancy interaction

Vacancies as point defects of missing atoms in lattice sites are ubiquitous in all materials. Furthermore, the H-vacancy interaction plays a crucial role in some mechanisms proposed to explain HE. Among these are the H-enhanced formation of strain-induced vacancies (HESIV) [1, 39], and a possible synergistic fracture mechanism with grain boundaries [40]. DFT studies show that Fe vacancies are able to trap up to six H atoms [3], which preferentially occupy sites close to the O-sites around the vacancy. The detailed energetics of V-Htrapping are complex; DFT calculations predict that the second H atom binds to a vacancy stronger if the vacancy already contains another H atom [3]. These observations make the H-V trapping mechanism a challenging but important benchmark for IAP performance.

The binding energy of subsequently added H within a

TABLE IV: Summary of the point-defect energetics of H in α -Fe given by DFT and the tested IAPs. $E_{s,X}^H$ is the solution energy of H in the three sites X=T, X=O, X=vac, or octahedral and tetrahedral interstitial sites, and in a Fe-vacancy, respectively. The subscript $\varepsilon\%$ refers to a hydrostatic engineering strain applied to the Fe lattice. The terms $E_{m,T-T}^H$ and $E_{m,T-O-T}^H$ are the energy barrier heights of the T-T and T-O-T transition paths calculated with CI-NEB.

	DFT	DFT (ZPE)	tabGAP	Ram_EAM	Wen_EAM	Kumar_EAM	Meng_NNIP
$\overline{E_{s,T}^H \text{ (eV)}}$	$0.228^{\rm a}\ 0.20^{\rm b}$	$0.30^{\rm b}\ 0.32^{\rm c}$	0.227	0.291	0.326	0.317	0.232
$E_{s,T,-2\varepsilon\%}^{H}$ (eV)	0.56^{d}	$0.67^{\rm e}$	0.559	0.564	0.590	0.629	0.601
$E_{s,T,+2\varepsilon\%}^{H}$ (eV)	$-0.036^{\rm d}$	$0.040^{\rm e}$	-0.033	0.055	0.096	0.089	-0.076
$E_{s,O}^{H}$ (eV)	$0.33^{\rm b}$	0.35^{f}	0.375	0.340	0.370	0.350	0.391
$\begin{array}{l} \overline{E_{s,T}^{H}\left(\text{eV}\right)} \\ E_{s,T,-2\varepsilon\%}^{H}\left(\text{eV}\right) \\ E_{s,T,+2\varepsilon\%}^{H}\left(\text{eV}\right) \\ E_{s,O}^{H}\left(\text{eV}\right) \\ E_{s,V}^{H}\left(\text{eV}\right) \end{array}$	-0.383^{g}	$-0.50^{\rm g}$	-0.350	-0.312	-0.284	-0.290	-0.367
$ E_{m,T-T}^{H} \text{ (eV)} \\ E_{m,T-T,-2\varepsilon\%}^{H} \text{ (eV)} $	$0.088^{\rm h} \ 0.090^{\rm g}$	$0.035^{\rm h} \ 0.044^{\rm g}$	0.114	0.041	0.044	0.027^*	0.107
$E_{m,T-T,-2\varepsilon\%}^{H'}$ (eV)	$0.095^{\rm d}$	$0.044^{\rm e}$	0.127	0.018	0.019	0.049^{*}	0.112
$E_{m,T-T,+2\varepsilon\%}^{H}$ (eV)	$0.072^{\rm d}$	$0.049^{\rm e}$	0.093	0.040	0.044	0.044^*	0.092
$E_{m,T-T,+2\varepsilon\%}^{H,T-T,+2\varepsilon\%} \text{ (eV)}$ $E_{m,T-O-T}^{H} \text{ (eV)}$	$0.148^{\rm g}$	$0.035^{\rm g}$	0.150	0.048	0.054^*	0.041^*	0.159
-	•						

^a This work ^b [35] ^c [34] ^d [33] ^e [31] ^f [37] ^g [3] ^h [38]

* Shape of the migration path does not agree with DFT.

vacancy can be defined as

$$E_b^{inc} = [E(H_T) - E(bulk)] - [E(H_n) - E(H_{n-1})], (5)$$

where H_T is a bulk α -Fe structure with a H atom in a Tsite, bulk refers to a pure α -Fe bulk structure, and H_n is a structure with n H atoms inserted into the vacancy. The results demonstrating the V-H-trapping with the tabGAP according to Eq. 5 are in shown in Tab. V. The insertion sites and the order in which the insertions were made were adopted from the supplemental information in Ref. [33]. Most notably, our tabGAP correctly reproduces the increase in binding energy from one to two H atoms in the vacancy from DFT results, and the strongly reduced binding energy of the sixth H atom. In contrast, this behavior is not captured by any of the classical EAMs, while the Meng_NNIP, which was also fit to the DFT data, shows a trend similar to that of DFT and tabGAP.

3. Interaction of H atoms with dislocations

We further verified the interactions of H atoms with dislocations using the Fe-H tabGAP. Since these interactions are also one of the possible culprits causing premature mechanical failure, it is important to ensure that the IAP adequately describes these interactions. Firstly, we identified the unique binding sites for H atoms around a $1/2\langle 111\rangle \{110\}$ easy-core screw dislocation. For this, we inserted H atoms randomly within a rectangular region of $5\times 5\times 3 \mbox{\normalfont\AA}$ around the dislocation core. These binding sites are illustrated in Fig. 2a and compared to the non-ZPE corrected DFT data from Ref. [41] in Fig. 2b. The binding sites in Fig. 2 are colored according to the binding energy values calculated with the tabGAP within the range defined by the colorbar on

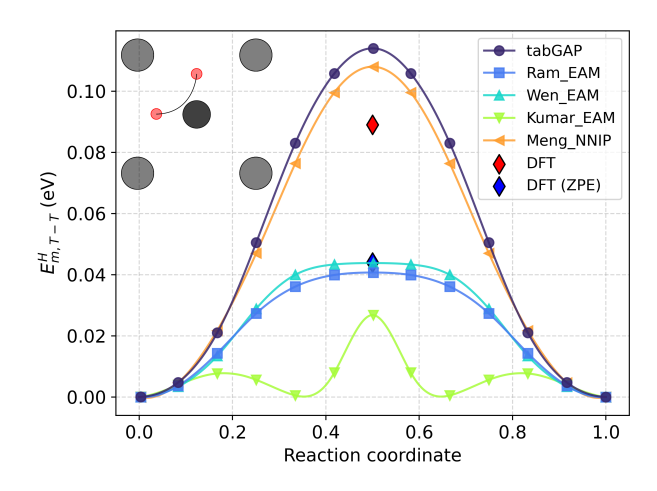
the side of the figure. The annotation of the binding sites is the same as in [41], hence for clarity, we do not show the DFT binding sites in Fig. 2a. The detailed comparison between the tabGAP and DFT binding sites, as well as those predicted by the classical IAP Ram_EAM, can be seen in the Appendix A. The absolute values of the tabGAP and DFT binding energy values for the annotated sites are compared in Fig. 2b. We see that the binding site locations with the tabGAP are well in line with the DFT predictions. Most notably, the three strongly binding basins around the dislocation core, those that include the E1 and E2 sites in the configuration E2-E1-E1-E2, are predicted by the tabGAP similarly to the DFT from Ref. [41], which is visible in Fig. A.1. In comparison, some of the binding site locations predicted by the classical IAPs are not in agreement with the locations identified in the DFT calculations.

Moreover, Fig. 2b shows a good quantitative agreement for the binding energies between tabGAP and DFT for all sites E1-E5. The binding energies within the E2-E1-E1-E2 basins differ from the DFT results by a few tens of meV, whereas the trend of very similar values of the binding energies within the basins remains similar in both calculations. The only substantial disagreement between tabGAP and DFT is the binding energy of the E0-site, where tabGAP reports a value of 0.26 eV, and DFT gives 0.085 eV. Here we note that our training set does not include structures with dislocations and H atoms simultaneously. These configurations were left out due to being bound to exaggerate the concentration of H atoms near the dislocation because of the limited size of the atomic configurations used for the training of the potential. Despite this, our potential is able to capture the H-dislocation interactions remarkably well. We attribute this to the strongly strained bulk α -Fe-H structure data containing local environments that are similar to dislocation cores.

TABLE V: The binding energy of incrementally added H in a single Fe vacancy. The H insertion sites and order were adopted from Ref. [33].

$\overline{E_b^{inc} \text{ (eV)}}$	n	$\mathrm{DFT^{a}}$	DFT (ZPE) ^a	tabGAP	Ram_EAM	Wen_EAM	Kumar_EAM	Meng_NNIP
	1	0.498	0.616	0.577	0.603	0.610	0.607	0.598
	2	0.543	0.651	0.608	0.603	0.572	0.578	0.616
	3	0.337	0.381	0.449	0.425	0.393	0.454	0.364
	4	0.304	0.351	0.451	0.361	0.327	0.348	0.338
	5	0.269	0.269	0.322	0.242	0.244	0.285	0.318
	6	-0.043	0.045	0.047	0.315	0.149	0.178	0.042

a [3]



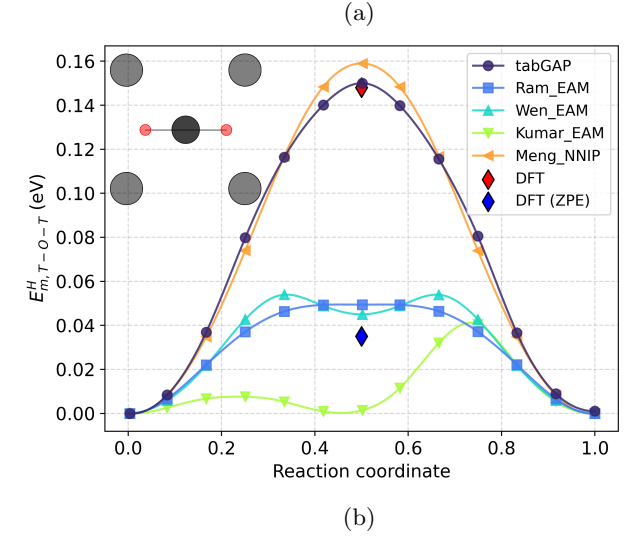


FIG. 1: The migration energy barriers of the T-T (1a) and T-O-T transitions (1b) for a H atom in bulk α-Fe, with sketches provided for both. DFT data is from Ref. [3]. The sketches show a [100]-view of the bcc unit cell. The H atoms are colored red, and Fe atoms are gray. DFT data is taken from Ref. [3].

In Fig. 3 we show the binding sites near a $1/2\langle1\,1\,1\rangle\{1\,1\,0\}$ edge dislocation. Here, the compressive stress region above and the tensile stress region below

are highlighted by the change of the color scale of the H binding sites in the upper (no-binding) and lower (binding) part of the lattice map in Fig. 3. The red triangle in the middle indicates the location of the dislocation core, which is also perpendicular to the plane of the figure as in the case of the screw dislocations in Fig. 2a. The glide plane of the dislocation separates the regions with the negative and positive binding energy H sites. An H atom strongly bonds within the tensile stress region with a maximum binding energy of $0.45\,\mathrm{eV}$ just below the glide plane layer of Fe atoms. This is in great agreement with Zhao and Lu's [42] QM/MM method calculation, which reported a maximum binding energy of $0.47\,\mathrm{eV}$ for the edge dislocation.

As can be seen in Fig. 3, strong binding sites are found throughout the entire search area. This is explained by the movement of the edge dislocation towards the inserted H atom during the structure's relaxation. This happened if the H atom was inserted into the tensile stress region, and in the compressive stress case, the dislocation was found to move away from the inserted H atom.

4. H-H interaction and clustering

Due to the limitations in spatial and temporal scales accessible within MD simulations, it is challenging to directly observe H-induced effects that may contribute to HE. This issue is commonly addressed in simulations by using significantly higher concentrations of H atoms than in experiments. While in the simulations, the concentrations can reach up to a few at.\% [4, 43-46, the experimentally observed concentrations of H atoms in bulk α-Fe are approximately 0.001 at.% even under H charging conditions [47, 48]. Hence, in simulations, special care must be taken to ensure that the chosen IAP describes the behavior of the H atoms in the condition of high H concentration fairly accurately. Song and Curtin [4] reported that the α-Fe-H IAP by Ramasubramaniam [31] spontaneously forms interstitial H-clusters in simulations at room temperature already at 1 at.%. They attributed this clustering to an unrealistic attractive interaction between H atoms occupying neighboring T-sites, as revealed in calculations

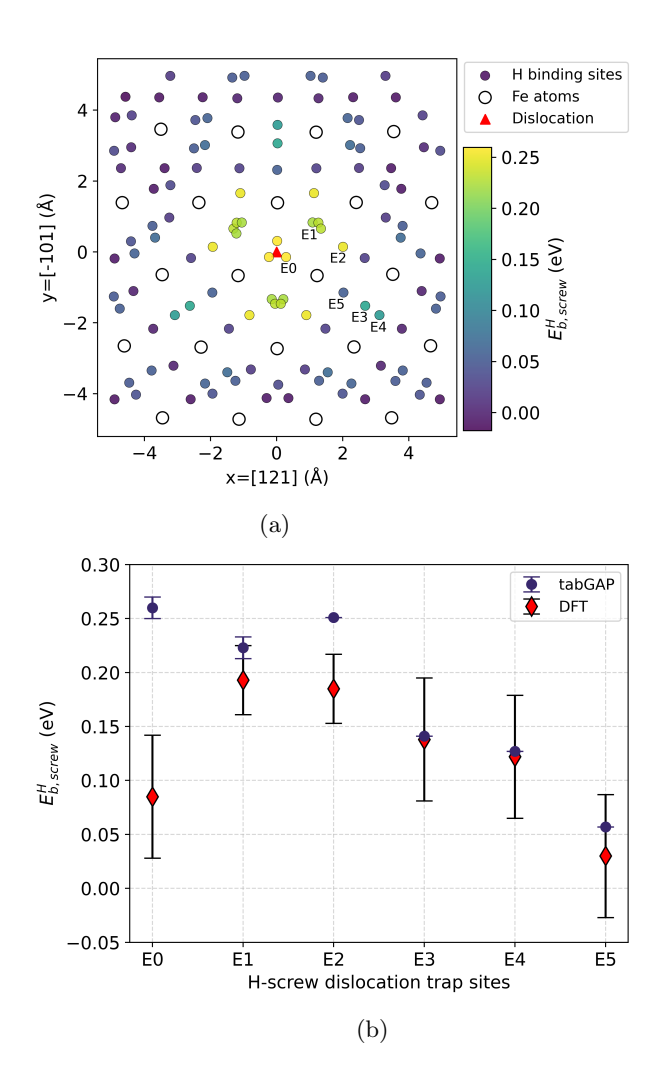


FIG. 2: The binding sites and energies for a H atom near a $1/2\langle 1\,1\,1\rangle \{1\,1\,0\}$ soft-core screw dislocation, calculated with the tabGAP (Fig. 2a), and the binding energies of a few annotated cites compared to DFT calculations done by Itakura *et al.* [41] (Fig. 2b).

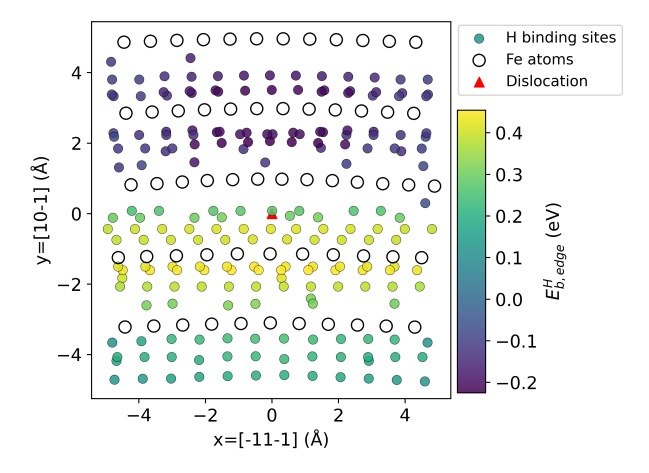


FIG. 3: The binding sites near a $1/2\langle 111\rangle\{110\}$ edge dislocation for a H atom, and their binding energies, calculated with the tabGAP.

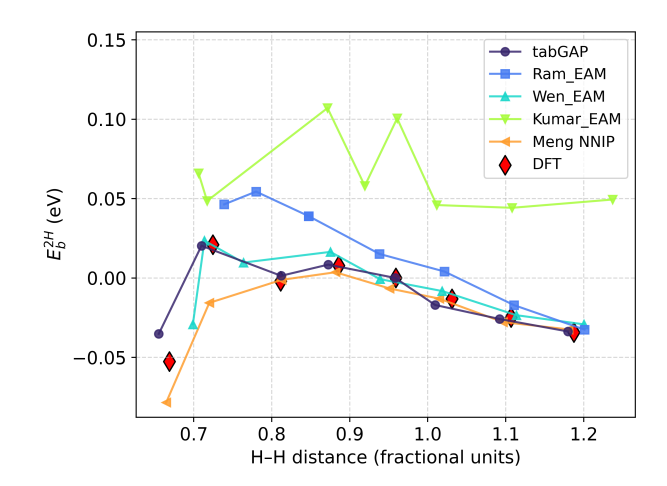


FIG. 4: The binding energy of interstitial H-pairs within the α-Fe matrix calculated with the Eq. 6. The x-axis is the distance (fractional units) between the pair of H atoms after energy minimization. DFT results are from Ref. [3].

of the pairwise binding energy (Eq. 6). Consequently, they modified the IAP by adding a repulsive H–H term (see supplementary information of Ref. [4]). However, even with the modified potential, Starikov *et al.* [43] observed the H clustering at concentrations above 2 at.% with this potential.

To evaluate the physical relevance of these simulation results, one can compare them with experimental data on iron hydride formation, where results indicate a threshold H concentration of 4–13 at.% [49–51], calculated from the approximate volume expansion caused by solute H. Therefore, based on the experimental evidence, H clustering in simulations with the concentration below the threshold of 4 at.% could be interpreted as an artifact of the selected IAP.

To quantitatively assess the prediction of H clustering by an IAP, we examine the binding energy of two interstitial H atoms using the following equation:

$$E_h^{2H} = 2E(H_T) - E(2H) + E(bulk), \tag{6}$$

where E(2H) is the energy of a structure containing two neighboring interstitial H atoms. A positive E_b^{2H} indicates a preferential occupation of closely located H sites relative to isolated H positions (H_T) . To assess the accuracy of the Fe–H tabGAP, the values of E_b^{2H} were calculated by placing H atoms into eight unique T-site pairs found within ~ 3 Å of each other in the α -Fe lattice (see Fig. 4), and relaxing the structure. The tabGAP accurately reproduces these binding energies obtained from DFT [3].

Taking into consideration only the E_b^{2H} values is insufficient for the proof of absence of clustering at low H concentrations because it only describes two neighboring H atoms in a zero-temperature environment. Therefore, we performed further test simulations at

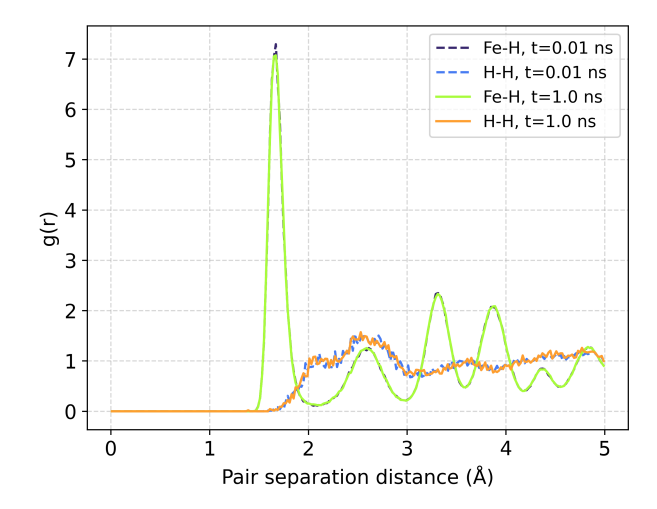


FIG. 5: The radial distribution functions of Fe-H and H-H pair separation distances in a $(37 \times 37 \times 37)$ -sized α -Fe 10 at.%-H-structure before and after equilibrating for 1 ns at 300 K with the NPT ensemble.

finite temperature with an interstitial H concentration range of 0.07-30 at.%. In these simulations, the H atoms were randomly distributed within $(10 \times 10 \times 10)$ sized α-Fe cells, and the structure was equilibrated at 300 K for 1 ns. The temperature and pressure within the structure were controlled via the NPT ensemble. The evolution of the H distribution was monitored following the radial distribution function (RDF) of H-pair separation distances. In these simulations no clustering of H atoms was observed, and the initial shape of the RDF did not change. To validate the accuracy of this result, we repeated the simulation for a larger $(37 \times 37 \times$ 37) cell and the H concentration of 10 at.%. The result is shown in Fig. 5. The mean displacement of the H atoms during this simulation was 33.13 Å, showing that the H atoms are mobile.

These simulations verify that the tabGAP is able to reliably predict the H–H interactions within an α -Fe lattice for the non-ZPE corrected dynamics, since its training dataset included numerous configurations with H concentrations between 10–20 at.%. Moreover, it accurately reproduces the interstitial H pair binding energies calculated with DFT, which is also in line with the conclusion of a low probability of H clustering within the Fe matrix. However, taking into account the ZPE correction might affect this conclusion significantly, as it increases the solution energy in α -Fe [3], and therefore most likely reduces solubility. This is, however, out of the scope of the present study.

5. Zero-temperature elastic moduli

The elastic moduli of α -Fe as a function of the concentration of H were calculated at $0\,\mathrm{K}$ by averaging

the results of simulations with α -Fe lattices containing different random distributions of H atoms. For each distribution, we randomly selected T-sites to be occupied by H atoms up to the target concentration. After the structure was loaded with the H atoms, it was relaxed using the conjugate gradient algorithm. For each H concentration 20 different H distributions were sampled.

The prepared structures were then deformed by applying the strain of $\varepsilon = 5 \times 10^{-3}$, and the elastic stiffness tensor was evaluated by measuring the change in the stress tensor. With the tabGAP, the lattice parameters were pre-calculated using the following linear equation:

$$a = 3.428 \times 10^{-5} T + 3.639 \times 10^{-3} cH + 2.82944 \text{ Å}, (7)$$

where T is the temperature in Kelvin and cH is the concentration of H in at.%. Eq. 7 was derived from a least-squares fit to lattice parameter data calculated with NPT simulations. The explanatory power of the fit was $R^2 = 0.9999$, indicating a very linear relationship. Similar equations were determined for all the other tested IAPs.

Figure 6 shows the trends of the C_{11} , C_{12} , and C_{44} dependencies on H concentration in the range of 0-5 at.% in comparison to DFT results [52]. There is a strong disagreement in the absolute values of C_{11} and C_{44} between the different models, while C_{12} agrees better between the different models. This is mainly explained by the fact that the EAM models are fit to the experimental elastic moduli values, which the DFT calculations disagree with by 10–18 % [53]. Overall, we see that the tabGAP results agree much better with those calculated by DFT in comparison to all the tested IAPs. For example, the linear dependencies of C_{11} and C_{44} on H concentration with the tabGAP have almost identical slopes to the DFT data. For C_{12} , tabGAP reproduces the DFT trend of a negative slope, though the absolute slope is smaller.

6. Finite-temperature elastic moduli

The finite-temperature dependencies of the elastic moduli of α -Fe with H concentration were obtained for the structures with lattice parameters calculated using Eq. 7 similarly to those constructed for the 0 K simulations. In this case, because of thermal fluctuations, the average change in the stress tensor of a deformed structure was sampled from an NVT simulation. To examine the chemical and volumetric effects of H on the elastic moduli separately, we additionally performed volume-equivalent calculations. In these calculations, the α -Fe lattice with the volume increased due to the H content of a given concentration was analyzed without the presence of H atoms in it.

Fig. 7 shows the thermal dependencies of the elastic moduli at various H concentrations. The tabGAP model predicts nearly linear decreases for all three elastic

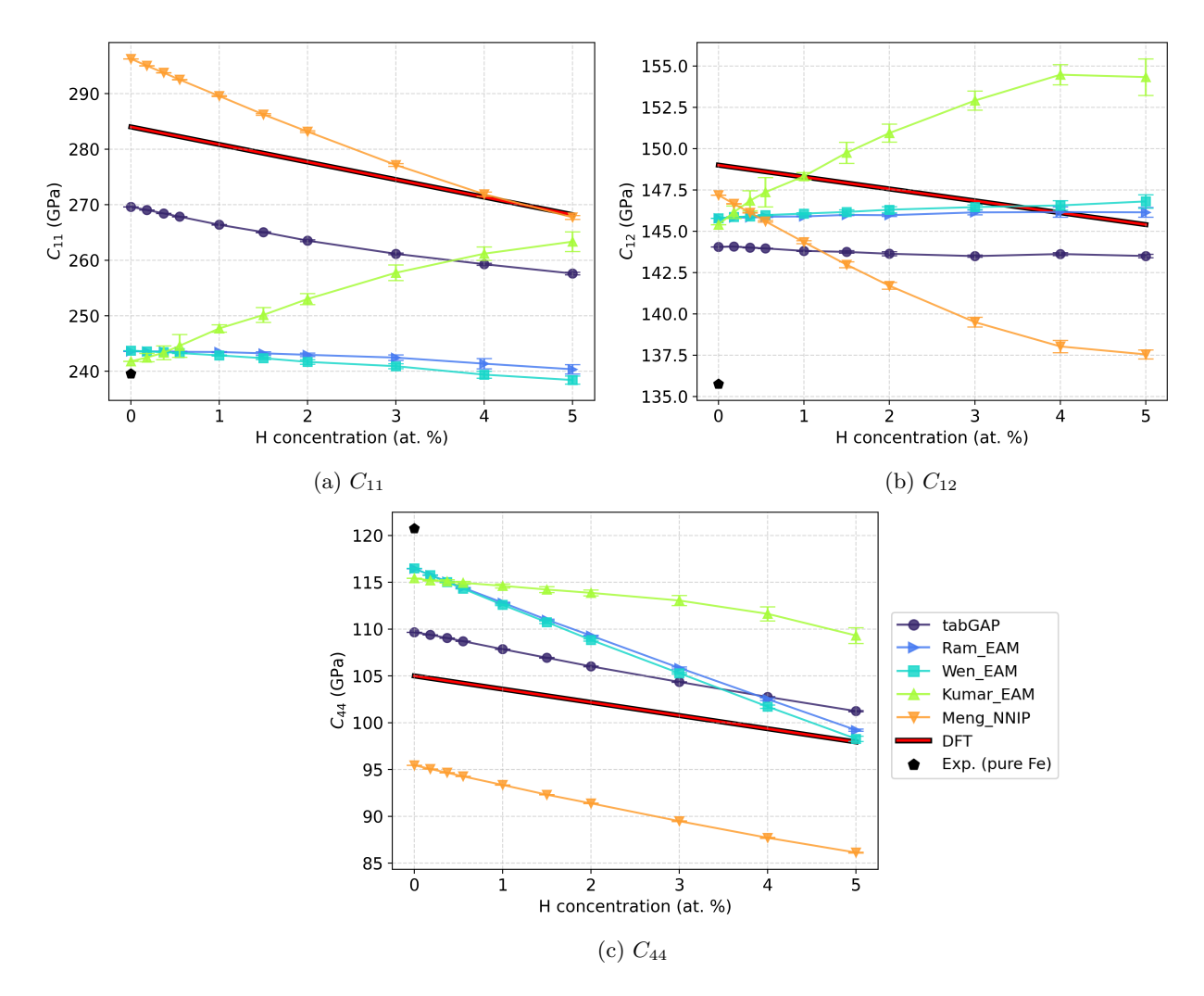


FIG. 6: The α-Fe-H elastic moduli of the tested IAPs at 0 K as a function of H concentration. The DFT results are linear best fits from Ref. [52].

moduli of pure α -Fe (dark-purple lines in Fig. 7). The effect of H remains negligible at H concentrations below ~ 1 at.%. At higher concentrations, we see a substantial decrease in both the C_{11} and C_{44} moduli, which decrease even stronger with further increase in the H content. In contrast, the effect of H concentration on C_{12} is opposite: the increased content of solute H atoms causes the increase of this modulus value with increasing temperature.

At room temperature, the H content decreases both C_{11} and C_{44} by $\sim 1.5 \%$, and increases C_{12} by $\sim 0.5 \%$ per 1 at.% increase in H concentration. Moreover, the volume-equivalent calculations for pure Fe indicated a more significant reduction for all three moduli per 1 at.% increase in H concentration; $\sim 2.3 \%$, $\sim 2.5 \%$, and $\sim 1.5 \%$ for C_{11} , C_{12} , and C_{44} , respectively. These results imply that the chemical contribution of H generally increases all three moduli, consistent with the DFT calculations by Psiachos et al. [52]. However, the decrease due to volumetric expansion is more significant

than the chemical contribution by H for C_{11} and C_{44} . While experimental results on single-crystal Fe samples is lacking, a decrease of 8% of the shear modulus (G) with 1 at.% H-content was deduced by Lunarska et~al. [54] for polycrystal α -Fe at 100 K. The tabGAP model predicts a decrease of 1.5% or 2.5% at this temperature, calculated with either $G = C_{44}$ or $G = (C_{11} - C_{12})/C_{11}$, respectively.

D. Effect of H on a α -Fe tensile test

To demonstrate the performance of the Fe-H tabGAP in a dynamic simulation related to HE, we simulated a tensile test by straining a perfect (unnotched), and a notched structure of α -Fe perpendicular to the notch plane, with and without the load of H atoms. A cell of $(30\times60\times5)$ unit cells was prepared for these simulations. The notch was created by removing the atoms within a biconvex lens-shaped volume with the major axis of

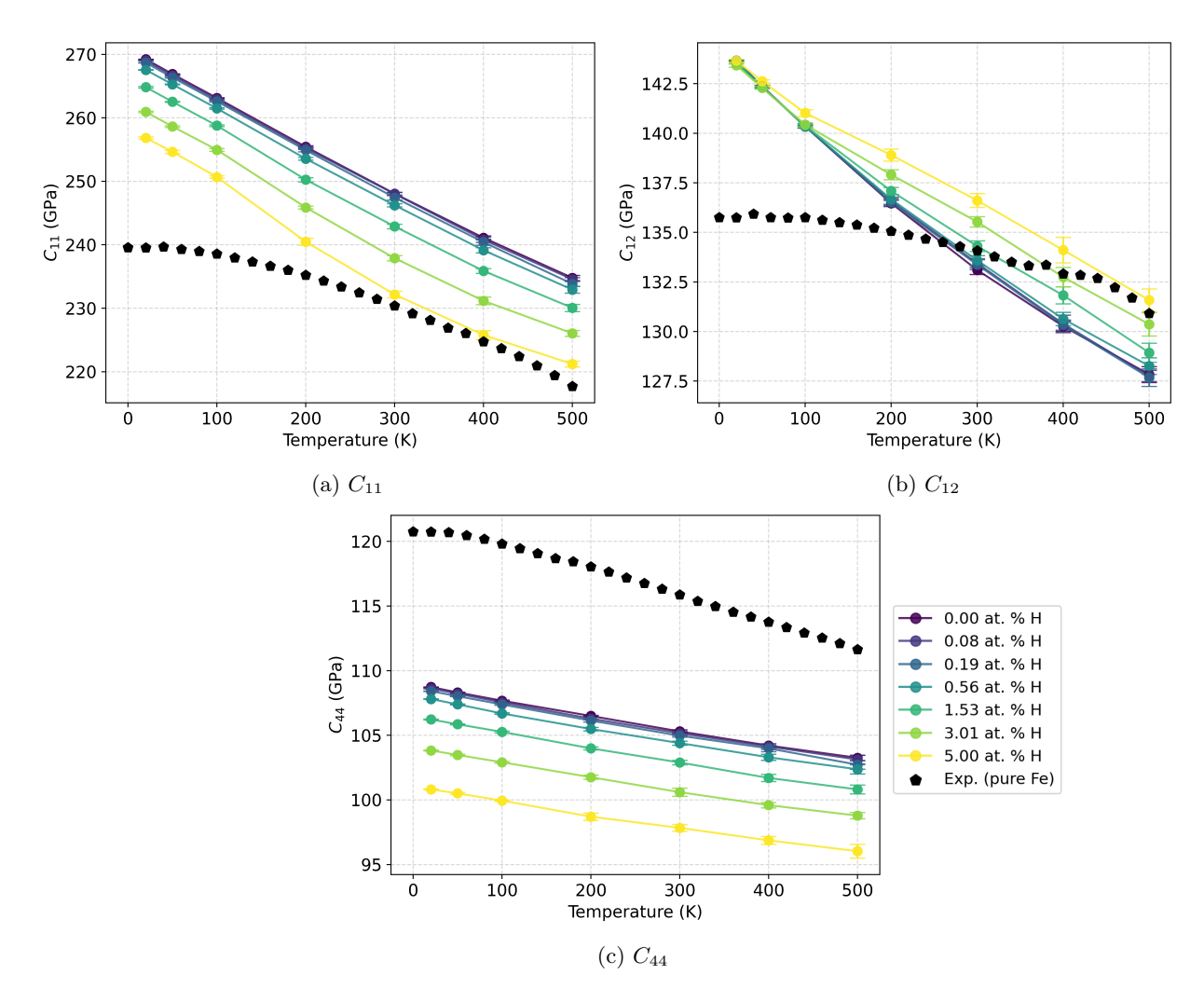


FIG. 7: The α-Fe-H elastic moduli for the tabGAP model as a function of both temperature and H concentration.

12.5 Å and the minor axis of 6.25 Å. The major axis was aligned with the $x=[1\,1\,\overline{2}]$ lattice direction, and the minor axis with the $y=[1\,1\,1]$ lattice direction, giving a $(1\,1\,1)[1\,1\,\overline{2}]$ notch geometry. This geometry includes a $\{1\,1\,\overline{2}\}\langle1\,1\,1\rangle$ dislocation slip system, and hence must be ductile. The z-axis of the structure was aligned with the $[1\,\overline{1}\,0]$ direction.

In total, four α -Fe structures were prepared for the tensile test simulations: a perfect and a notched structure, each in a H-free and a H-charged state. In the H-charged cases, 1 at.% hydrogen was introduced with atoms randomly distributed in the structure. All structures were then equilibrated for 400 ps before applying strain to allow hydrogen to redistribute.

The equilibrated structures were then subjected to the mode I tensile load in the y-direction at 300 K in a stepwise manner. At each step, the structure was strained for 125 ps at the rate of $\dot{\varepsilon} = 1 \times 10^8 \, \mathrm{s}^{-1}$, followed by a 20 ps equilibration phase to allow the structure to adjust to the current strain value. The strain was increased until the total value of $\varepsilon = 0.25$, or up to total

failure of the structure.

To quantify the effect that the H load had on the structure during the tensile test, we followed the yycomponent of the pressure tensor, the tensile stress, in Fig. 9. We also tracked the number of formed glissile dislocations with DXA implemented in Ovito [55], counting them manually. In some instances, DXA reported cessile, and flickering, dislocation-type defects in severely deformed regions of the structure. These were disregarded as artifacts. Furthermore, the number of vacancies that formed inside the bulk of the structure were calculated with Wigner-Seitz defect analysis (WS) [56]. The site occupancies reported by WS were time-averaged over an equilibration phase, and sites with average occupancy less than 0.5 were counted as vacancies. The reference structure for WS was a relaxed pure Fe cell, strained at $\varepsilon = 0.1$. Any vacancies near the free surfaces were discounted due to the WS method failing to accurately report occupancies there due to the differing strains between the reference and the analyzed structures.

Fig. 8 shows the snapshot of the notched structure at the end of the equilibration simulation. Although the H atoms were initially placed in the stable T-sites of the lattice, already the initial equilibration simulation promoted redistribution of the H atoms. The colored lines in Fig. 8 illustrate the active migration of H atoms between the Fe atoms toward the preferred location for H atoms at the tip of the notch along the entire length of the trough in the z direction. We found that all five sites available along the z direction of the structure at the tip of the notch were occupied by H atoms. Out of these, three diffused to the notch tip from the bulk. The other two diffused to this location along the upper surface of the notch, where they were randomly placed at the start of the simulation. It is clear that the notch tip acts as a deep trap for the H atoms, since they arrived and stayed in this region during the fairly long equilibration phase.

Fig. 9 shows the stress-strain curves generated from the mode I tensile tests for all of the four structures. As can be seen, both notched structures experienced fracture, although the Fe-H structure failed significantly earlier, at $\varepsilon=0.069$ vs. $\varepsilon=0.077$, indicating H enhanced embrittlement of the α -Fe lattice. Fig. 10 shows the mechanism by which the H atoms cause earlier crack propagation in the notched structure. Although we chose the notch geometry to align with a $\{11\bar{2}\}\langle111\rangle$ dislocation slip system, no dislocations (or other defects) were observed at any point in these structures. As can be seen in the snapshots in Fig. 10, the H atoms accumulate at the tip, filling the opening at its tip, and causing brittle failure before a dislocation has time to form.

Fig. 10 shows the configuration of the notch tip just before, during, and after the start of the propagation of the crack. It can be seen in Fig. 10b how the H atoms positioned at the notch tip initiate the propagation of a crack by cleaving apart the plane of Fe atoms ahead of the notch tip. This cleaving action then causes a chain reaction of further dissociating Fe atom planes, leading to the crack propagating. The H atoms initially at the notch tip follow the propagation up to $\sim 15 \,\text{Å}$ into the material, and then reaching free surface sites (Fig. 10d).

In the Appendix B, we show snapshots of the evolution of the perfect Fe-H and Fe structures, see Figs. B.2 and B.3, respectively. With no initial notch, the four corners of the rectangularly shaped structure acted as the initial yield points due to shear stress concentrating there. The first plastic events were observed at $\varepsilon =$ 0.0917 vs. $\varepsilon = 0.093$ (Figs. B.2a and B.3a) for the Fe-H and Fe structures, respectively, with the emission of $\langle 100 \rangle$ -type edge dislocations from the top left and bottom right corners. Immediately after this, $1/2\langle 111\rangle$ type dislocations were emitted from the bottom left and top right corners. In total, twelve dislocations were observed in both structures before failure and there was no evidence of a change in plasticity by H-loading the α -Fe structure. The cumulative number of dislocations can be seen in Fig. 13, which show very similar dependencies for H-free and H-loaded Fe structures.

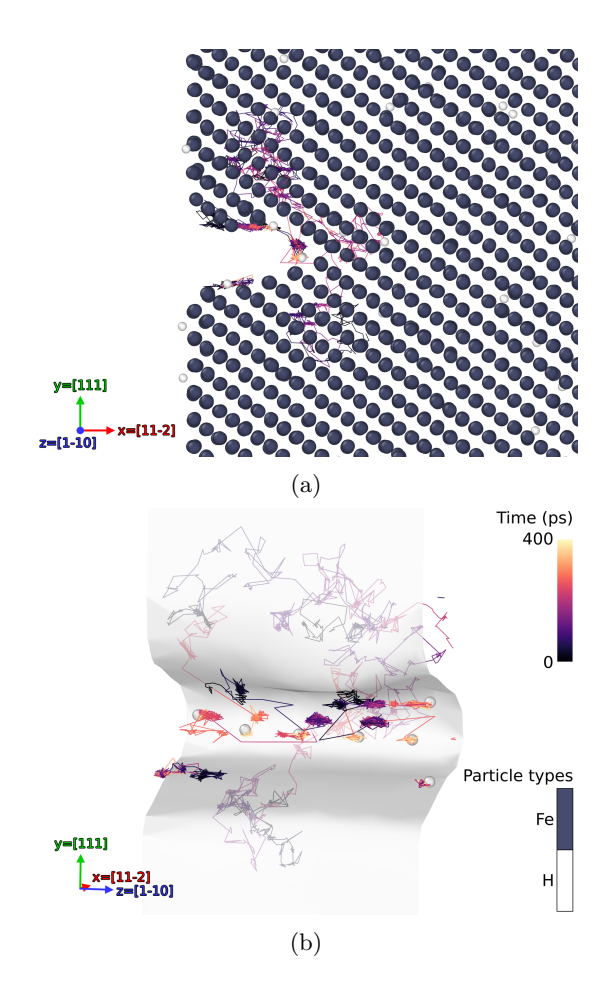


FIG. 8: H atom positions at the end of the equilibration, and their trajectories during it, close the α -Fe notch. Trajectory lines are colored according to the passed simulation time. In Fig. 8b the notch is shown from the front with the Fe atoms hidden, and the defect mesh surface calculated by DXA in Ovito is shown [57].

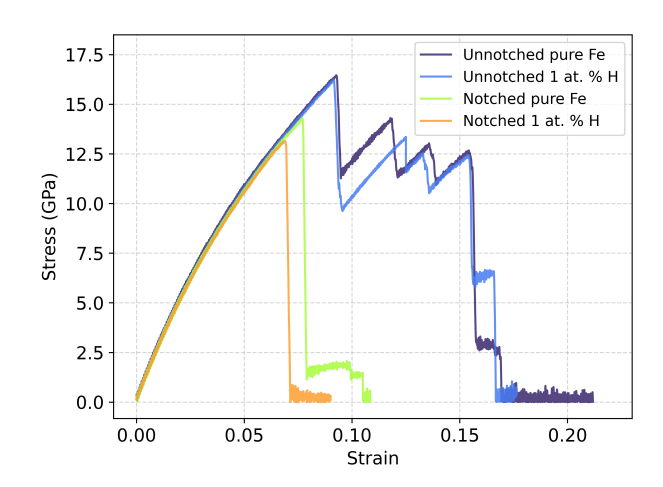


FIG. 9: The stress-strain curves from the four different α -Fe tensile tests with and without a notch or H.

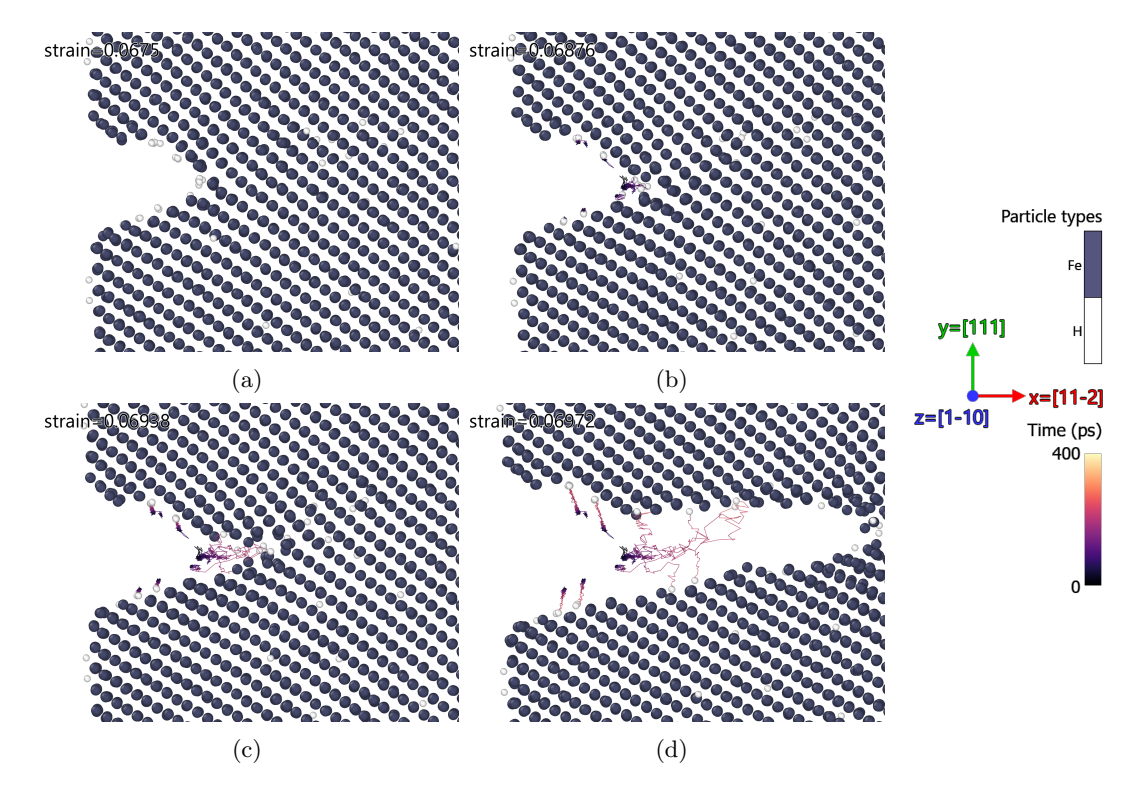


FIG. 10: H atom positions and trajectories before (10a), during (10b and 10c), and after (10d) crack propagation at the notch tip.

Both perfect (unnotched) structures failed via crack propagation that began from one of the corners, at the bottom right for the Fe-H, and at the top left for the pure Fe (Figs. B.2d and B.3d). The formation of the crack was preceded by the formation of a void caused by cumulative plastic deformation. As can be seen from the stressstrain curves for both structures (Fig. 9), there was no significant H-induced effect on mechanical failure in the unnotched structures. However, a marked increase in the number of vacancy-type defects was observed in the Fe-H structure. These extra vacancies were generated by the dislocation-dislocation or dislocation-H interaction, leading to the formation of 22 vacancies, which is three times the number of vacancies formed in the pure Fe (only 7 vacancies at the end of the simulation). demonstrate the mechanism of a vacancy formation due to H-dislocation interactions, we selected two exemplary events which are shown in Figs. 11 and 12. Fig. 11(af) shows the subsequent snapshots of a 1/2(111) edge dislocation (the green line shows the dislocation core, which is perpendicular to the plane of the image) that encounters two H atoms (small gray balls in the images). The arrows show the displacements of atoms from their locations in an initial frame to the locations in the current snapshot. After the dislocation passes through these atoms, a vacancy appeared as a result of this interaction. In Fig. 12, we show a $\langle 100 \rangle$ edge dislocation that encounters two H atoms, leaving behind a (113) trivacancy $(V_3(113))$ [58].

In Figs. 11a-11b the approach of the $1/2\langle 1\,1\,1\rangle$ edge dislocation to the two H atoms is shown. In Figs. 11c-11d it can be seen how the H atoms have disrupted the normal glide of the dislocation by blocking an Fe atom (highlighted with a dark hue) from relaxing to its expected antiparallel-to-glide direction. The Fe atom then relaxes to the parallel-to-glide direction instead, forming a vacancy before it, and an interstitial in the form of a crowdion after it. The crowdion migrates forward alongside the dislocation core. In Figs. 11e-11f the first three Fe atoms in the crowdion can be seen relaxing back to the antiparallel-to-glide configuration, which moves the vacancy three atomic spacings forward to its final stable configuration.

A similar mechanism of action can be seen in Fig. 12 for the formation of the $V_3(113)$ defect. The gliding $\langle 100 \rangle$ -dislocation core contains a larger open volume which the H atoms migrate into at the arrival of the dislocation. The H atoms then prevent the following Fe atoms from relaxing into the antiparallel-to-glide direction, and closing the volume. The result is the $V_3(113)$ defect, with three crowdions propagating along the dislocation and later annihilating at the free surface of the simulation cell, close to the bottom right corner of structure shown in Fig. B.2.

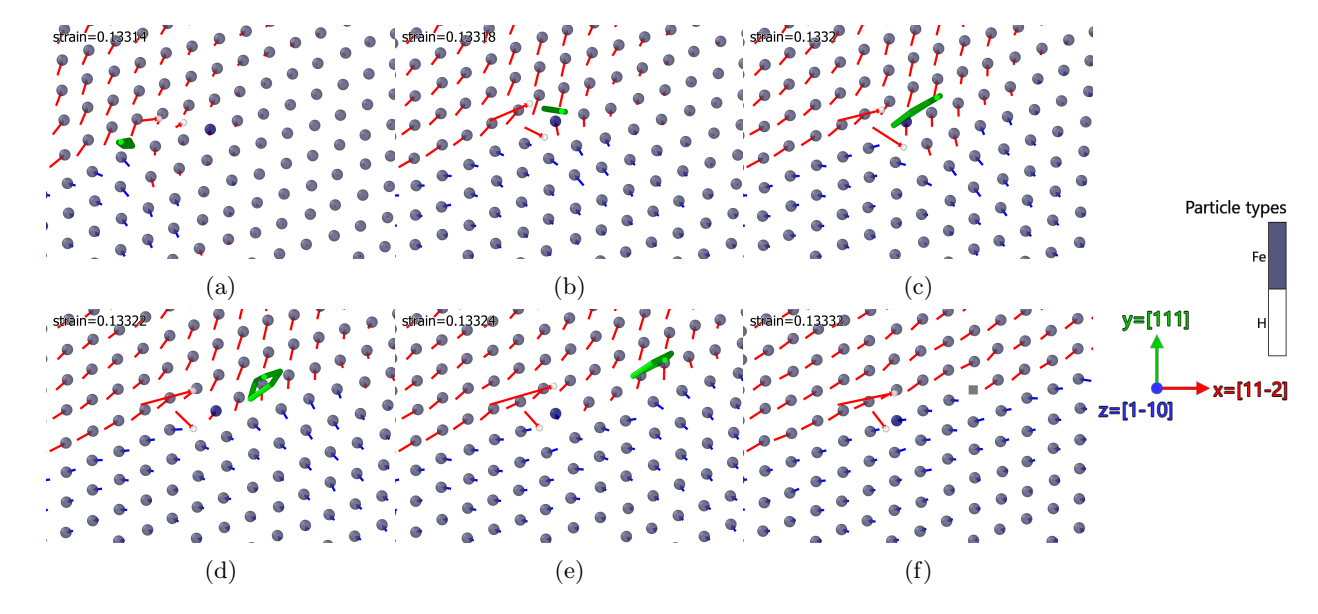


FIG. 11: (a)-(f) A series of snapshots from the unnot ched α -Fe-1 at.%-H tensile test simulation. A $1/2\langle 1\,1\,1\rangle$ -dislocation encounters two H atoms, and creates a single vacancy (a gray square in the last snapshot (11f)). Only the Fe atoms in the (110)-plane of the V_1 , and the two nearby H atoms, are shown. A single Fe atom is highlighted with a darker hue for reference. The displacements of the atoms are shown with color coding according to the displacement direction; red vectors are the atomic displacements which point in the direction of the dislocation glide, and blue vectors are displacements in the opposite direction. The displacements show the unscaled distance between the atom's location in an initial frame and the current one.

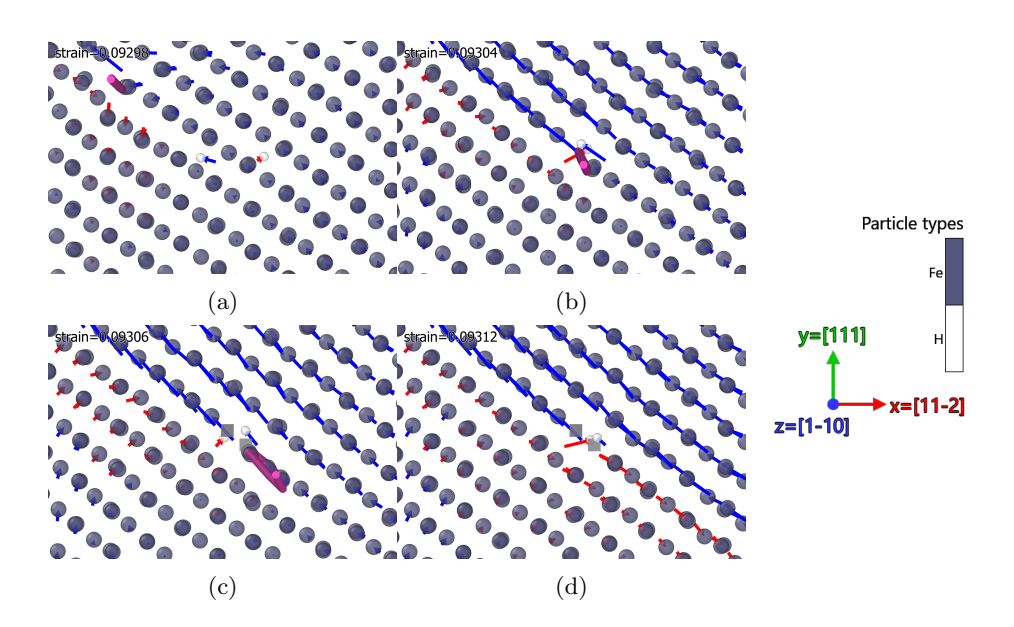


FIG. 12: (a)-(d) A series of snapshots from the unnotched α -Fe-1 at.%-H tensile test simulation. A $\langle 1\,0\,0 \rangle$ -dislocation encounters two H atoms, and creates a $V_3(1\,1\,3)$ -defect (gray squares in the last two snapshots (12c-12d). Only the Fe atoms in the (110)-planes of the $V_3(1\,1\,3)$, and the two nearby H atoms, are shown. The displacements of the atoms are shown with color coding according to the displacement direction; red vectors are the atomic displacements which point in the direction of the dislocation glide, and blue vectors are displacements in the opposite direction. The vacancy sites are marked with gray squares.

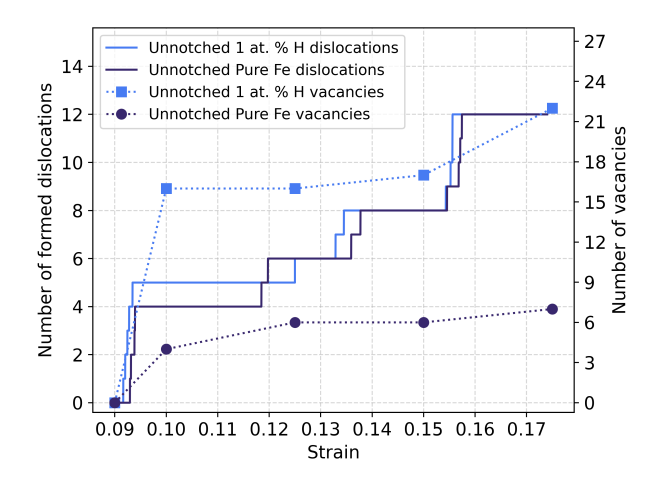


FIG. 13: The number of formed dislocations (solid lines), and the number of formed vacancies (markers and dashed lines) in the unnotched tensile test simulations. The dislocations were counted using DXA [57], and the vacancies were counted with Wigner-Seitz defect analysis.

IV. DISCUSSION

In this section, we further discuss the results we obtained in the tensile test simulations using the developed Fe-H tabGAP.

As we saw in Sec. III D, crack propagation was initiated much earlier in the simulations of tensile tests of a H-loaded notched α -Fe structure compared to the similar, but H-free structure. We assigned this effect to the accumulation of H at the tip of the notch. This simulation result suggests that at high strain rates in α -Fe structures HE is mainly caused by the H-enhanced decohesion (HEDE) mechanism. H promotes earlier brittle fracture by filling the space between the Fe atoms, enhancing their decohesion at the tip of the notch. This finding is in agreement with the HEDE model proposed by Vehoff et~al.~[59] based on the experimental results in Fe-2.6%Si and in Ni [60, 61].

Although the $(111)[11\overline{2}]$ notch geometry was specifically selected to allow plastic events to occur through the $\{11\overline{2}\}\langle111\rangle$ slip system, no dislocations were observed in the notched tensile test simulations. Additionally to seeing mechanical failure taking place in the notched structures at lower strains, the failure mode of cleavage fracture is likely to be explained by the high strain rate used in our study, $\dot{\varepsilon}=1\times10^8\,\mathrm{s^{-1}}$, due to limitations of MD simulations [33, 46, 62]. It has been experimentally observed that the brittle failure mode becomes more probable with increasing strain rate in α -Fe [63].

We note here that multiple MD studies of α -Fe crack propagation during tensile test simulations, with and without H, have reported "bcc-to-fcc transformation"-type phenomena ahead of crack tips [4, 46, 62, 64, 65].

The work by Möller et al. [40, 66] demonstrated that these findings are in fact planar faults emanating from the crack tip, which are likely artifacts of the used EAM IAPs. We note that we did not observe such planar stacking faults in our simulations with the presently developed tabGAP, which is also in line with experimental and DFT results, which do not confirm formation of such faults [40, 66].

In the tensile tests simulated for the unnotched structure, we observed that the solute H atoms increase vacancy concentration, with the vacancies forming via an interaction with gliding dislocations. This finding suggests that the hydrogen-enhanced strain-induced vacancies (HESIV) mechanism of HE [1, 39] might be significant. Our finding is also supported by experimental positron lifetime spectroscopy evidence of an increase in the concentration of vacancies after plastic deformation in H⁻ charged α-Fe [67]. Some previous MD studies have reported evidence of HESIV for the α -Fe-H system as well [68, 69]. However, the vacancy formation mechanism that we present may be affected by the exaggerated concentration of H atoms and stresses which are far from the conditions in typical experiments. Despite this, the mechanism of vacancy formation affected by the presence of H atoms in the lattice may take place in experimental conditions, as we can see in frame-by-frame resolution (Figs. 11 and 12) in our simulations how a H atom can create additional local strain inside the dislocation core, resulting in a glide-disrupting displacement of an Fe atom, leaving a vacancy behind.

V. CONCLUSIONS

In this work, we present a new machine-learned interatomic potential (tabGAP) for the α-Fe-H system based on a Density Functional Theory (DFT) generated dataset of atomic structures, forces, and energies. We have quantified the accuracy of the tabGAP model via benchmarking it against DFT, and many of the other currently published α -Fe-H potentials in H-point defect energetics, H-vacancy interaction, H-dislocation interaction, H-H interaction in the α -Fe matrix, and the effect of H on the α-Fe elastic moduli. Most notably, the tabGAP model agrees well with the experimental and computational literature on the effect of H on the shear modulus of α -Fe, predicting a decrease of $\sim 2\%$ with a Hcontent of 1 at.%. The presented tabGAP model strikes a new balance between accuracy and performance, offering near-DFT accuracy in the benchmarked properties, while having a computational cost close to that of the classical EAM potentials.

Furthermore, we applied the developed tabGAP model in molecular dynamics simulations of a tensile test for bulk and the $(1\,1\,1)[1\,1\,\overline{2}]$ notched α -Fe structure with and without a H load. In these simulations, we observed the following:

• Hydrogen accumulates in the notch tip, and

initiates earlier crack propagation via a decohesive interaction on the notch tip Fe atoms. This finding is in agreement with experimental results.

• Hydrogen can promote the formation of vacancies via disrupting the glide of edge dislocations, leading to higher vacancy concentrations, and enhanced embrittlement.

As the presented tabGAP model and its training dataset have been demonstrated to offer excellent performance and accuracy for the α -Fe-H system, it lays the groundwork for future augmentations, and large-scale hydrogen embrittlement simulations.

ACKNOWLEDGMENTS

This work was funded by the European Union under Grant Agreement n° 101135374. Views and opinions expressed are however those of the author(s) only and do not necessarily reflect those of the European Union or the European Health and Digital Executive Agency (HADEA). Neither the European Union nor the granting authority can be held responsible for them. A.L.C. acknowledges the AI4S fellowship within the "Generación D" initiative by Red.es, Ministerio para la Transformación Digital y de la Función Pública, for talent attraction (C005/24-ED CV1), funded by NextGenerationEU through the Recovery, Transformation and Resilience Plans (PRTR). The authors would like to thank the CSC-IT Center for Science and the Finnish Computing Competence Infrastructure (FCCI) for providing the computational and data storage resources for this work.

APPENDICES

Appendix A: Binding sites of H to a screw dislocation

The H binding site positions around a $1/2\langle 1\,1\,1\rangle\{1\,1\,0\}$ easy-core screw dislocation given by the presented Fe-H tabGAP and the Ram_EAM models are compared to the sites reported by Itakura et al. [41]. As the α -Fe lattice parameters of these models differ from each other, the H binding site positions were scaled by matching the positions of the three central dislocation core Fe atoms. From Fig. A.1 we can see excellent agreement in the binding site positions between the tabGAP and DFT, while there are larger differences between DFT and Ram_EAM. The Ram_EAM also reports three additional high- E_b sites located next to the screw dislocation core which don't exist in the DFT and tabGAP results.

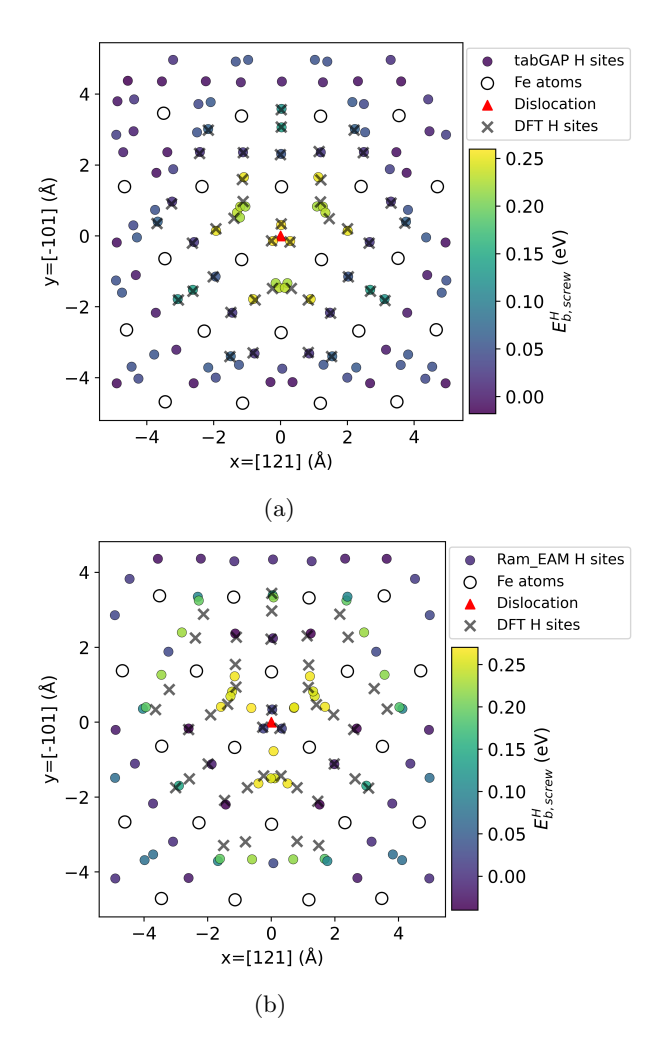


FIG. A.1: The binding sites and energies for a H atom near a $1/2\langle 1\,1\,1\rangle\{1\,1\,0\}$ soft-core screw dislocation, calculated with the tabGAP (Fig. A.1a) and Ram_EAM (Fig. A.1b). In addition, the binding sites given by DFT (reproduced from Fig. 6a in Ref. [41]) are marked on top with gray crosses.

Appendix B: Tensile test strain profile and evolution figures

We give qualitative snapshots of the microstructural evolution of the unnotched tensile test simulations for the pure and 1 at.%-H-loaded in α -Festructures in Figs. B.2 and B.3, respectively.

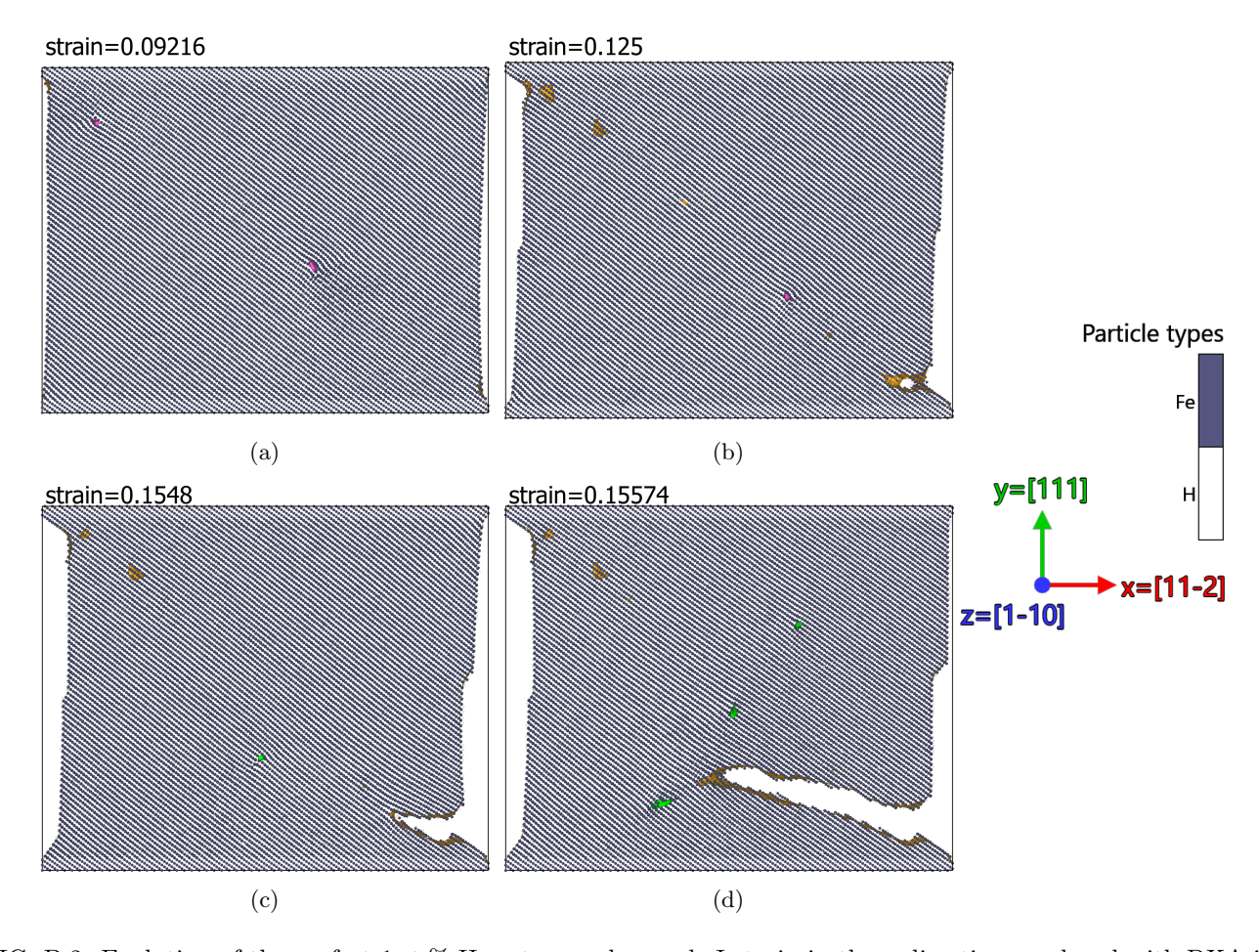


FIG. B.2: Evolution of the perfect 1 at.% H system under mode I strain in the y-direction, analyzed with DXA in Ovito [57]. $\langle 1\,0\,0 \rangle$ -type dislocations are colored pink, and $1/2\langle 1\,1\,1 \rangle$ -type dislocations are colored green. The orange surfaces are the defect mesh output by DXA. In Fig. B.2a a moment after the first dislocations ($\langle 1\,0\,0 \rangle$) are emitted is shown. In Fig. B.2b a near-surface void has formed at the lower right corner of the system. In Fig. B.2c the void has opened up, and acts as a crack initiation site. In Fig. B.2d the propagating crack has emitted three $1/2\langle 1\,1\,1 \rangle$ edge dislocations.

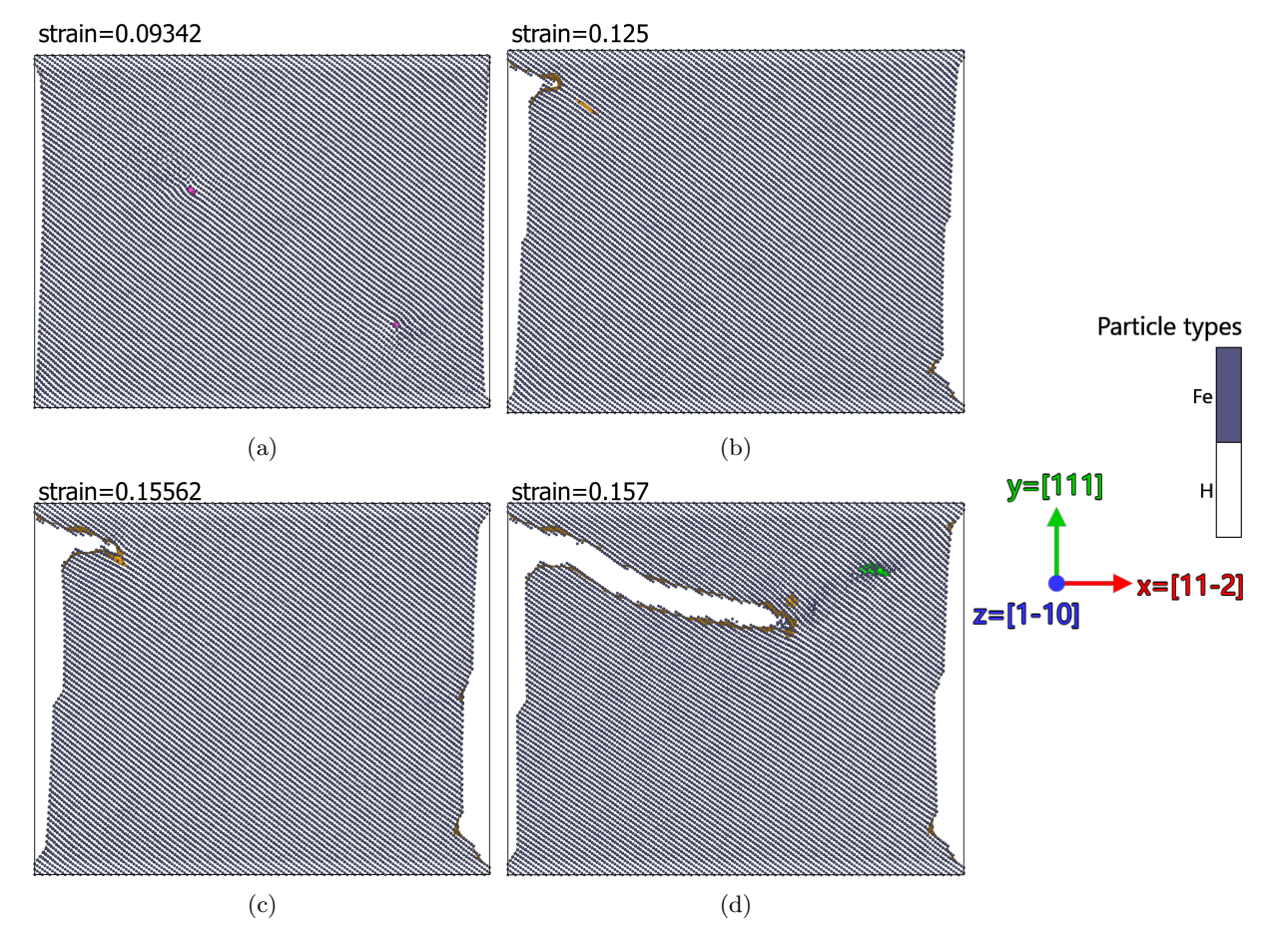


FIG. B.3: Evolution of the perfect pure Fe system under mode I strain in the y-direction, analyzed with DXA in Ovito [57]. $\langle 1\,0\,0 \rangle$ -type dislocations are colored pink, and $1/2\langle 1\,1\,1 \rangle$ -type dislocations are colored green. The orange surfaces are the defect mesh output by DXA. In Fig. B.3a a moment after the first dislocations ($\langle 1\,0\,0 \rangle$) are emitted is shown. In Fig. B.3b a near-surface void has formed at the lower right corner of the system. In Fig. B.3c the void has opened up, and acts as a crack initiation site. In Fig. B.3d the propagating crack has emitted a single $1/2\langle 1\,1\,1 \rangle$ edge dislocation.

- [1] H. Yu, A. Díaz, X. Lu, B. Sun, Y. Ding, M. Koyama, J. He, X. Zhou, A. Oudriss, X. Feaugas, and Z. Zhang, Hydrogen Embrittlement as a Conspicuous Material Challenge-Comprehensive Review and Future Directions, Chemical Reviews 124, 6271 (2024).
- [2] I. M. Robertson, P. Sofronis, A. Nagao, M. L. Martin, S. Wang, D. W. Gross, and K. E. Nygren, Hydrogen Embrittlement Understood, Metallurgical and Materials Transactions B 46, 1085 (2015).
- [3] E. Hayward and C.-C. Fu, Interplay between hydrogen and vacancies in alpha-Fe, Physical Review B 87, 174103 (2013).
- [4] J. Song and W. A. Curtin, Atomic mechanism and prediction of hydrogen embrittlement in iron, Nature Materials 12, 145 (2013).
- [5] L. Fu and H. Fang, Atomistic investigation of hydrogen embrittlement effect for symmetric and asymmetric grain boundary structures of bcc Fe, Computational Materials Science 158, 58 (2019).
- [6] X. Xing, R. Cheng, G. Cui, J. Liu, J. Gou, C. Yang, Z. Li, and F. Yang, Quantification of the temperature threshold of hydrogen embrittlement in X90 pipeline steel, Materials Science and Engineering: A 800, 140118 (2021).
- [7] P. Kumar, M. M. Ludhwani, S. Das, V. Gavini, A. Kanjarla, and I. Adlakha, Effect of hydrogen on plasticity of alpha-Fe: A multi-scale assessment, International Journal of Plasticity 165, 103613 (2023).
- [8] R. Matsumoto, S. Taketomi, S. Matsumoto, and N. Miyazaki, Atomistic simulations of hydrogen embrittlement, International Journal of Hydrogen Energy 34, 9576 (2009).
- [9] B. Mortazavi, X. Zhuang, T. Rabczuk, and A. V. Shapeev, Atomistic modeling of the mechanical properties: the rise of machine learning interatomic potentials, Materials Horizons 10, 1956 (2023).
- [10] L. Zhang, G. Csányi, E. van der Giessen, and F. Maresca, Efficiency, accuracy, and transferability of machine learning potentials: Application to dislocations and cracks in iron, Acta Materialia 270, 119788 (2024).
- [11] J. Byggmästar, G. Nikoulis, A. Fellman, F. Granberg, F. Djurabekova, and K. Nordlund, Multiscale machinelearning interatomic potentials for ferromagnetic and liquid iron, Journal of Physics: Condensed Matter 34, 305402 (2022).
- [12] J. Byggmästar, Simple machine-learned interatomic potentials for complex alloys, Physical Review Materials 6, 10.1103/PhysRevMaterials.6.083801 (2022).
- [13] A. Fellman, J. Byggmästar, F. Granberg, F. Djurabekova, and K. Nordlund, Radiation damage and phase stability of $\mathrm{Al}_x\mathrm{CrCuFeNi}_y$ alloys using a machine-learned interatomic potential (2025), arXiv:2503.07344 [cond-mat].
- [14] Y. Zuo, C. Chen, X. Li, Z. Deng, Y. Chen, J. Behler, G. Csányi, A. V. Shapeev, A. P. Thompson, M. A. Wood, and S. P. Ong, Performance and Cost Assessment of Machine Learning Interatomic Potentials, The Journal of Physical Chemistry A 124, 731 (2020).
- [15] A. P. Bartók, Gaussian Approximation Potentials: The Accuracy of Quantum Mechanics, without the Electrons, Physical Review Letters 104,

- 10.1103/PhysRevLett.104.136403 (2010).
- [16] A. P. Bartók, On representing chemical environments, Physical Review B 87, 10.1103/PhysRevB.87.184115 (2013).
- [17] J. Byggmästar, A. Hamedani, K. Nordlund, and F. Djurabekova, Machine-learning interatomic potential for radiation damage and defects in tungsten, Physical Review B 100, 144105 (2019).
- [18] J. F. Ziegler and J. P. Biersack, The Stopping and Range of Ions in Matter, in *Treatise on Heavy-Ion Science:* Volume 6: Astrophysics, Chemistry, and Condensed Matter, edited by D. A. Bromley (Springer US, Boston, MA, 1985) pp. 93–129.
- [19] K. Nordlund, N. Runeberg, and D. Sundholm, Repulsive interatomic potentials calculated using Hartree-Fock and density-functional theory methods, Nuclear Instruments and Methods in Physics Research Section B: Beam Interactions with Materials and Atoms 132, 45 (1997).
- [20] S. Klawohn, J. P. Darby, J. R. Kermode, G. Csányi, M. A. Caro, and A. P. Bartók, Gaussian approximation potentials: Theory, software implementation and application examples, The Journal of Chemical Physics 159, 174108 (2023).
- [21] G. Kresse and J. Furthmüller, Efficiency of ab-initio total energy calculations for metals and semiconductors using a plane-wave basis set, Computational Materials Science 6, 15 (1996).
- [22] G. Kresse and J. Furthmüller, Efficient iterative schemes for ab initio total-energy calculations using a plane-wave basis set, Physical Review B 54, 11169 (1996).
- [23] G. Kresse and J. Hafner, Ab initio molecular dynamics for liquid metals, Physical Review B 47, 558 (1993).
- [24] G. Kresse and J. Hafner, Ab initio molecular-dynamics simulation of the liquid-metal-amorphous-semiconductor transition in germanium, Physical Review B 49, 14251 (1994).
- [25] J. P. Perdew, K. Burke, and M. Ernzerhof, Generalized Gradient Approximation Made Simple, Physical Review Letters 77, 3865 (1996).
- [26] G. Kresse and D. Joubert, From ultrasoft pseudopotentials to the projector augmented-wave method, Physical Review B 59, 1758 (1999).
- [27] J. Byggmästar, K. Nordlund, and F. Djurabekova, Modeling refractory high-entropy alloys with efficient machine-learned interatomic potentials: Defects and segregation, Physical Review B 104, 104101 (2021).
- [28] A. P. Thompson, H. M. Aktulga, R. Berger, D. S. Bolintineanu, W. M. Brown, P. S. Crozier, P. J. in 't Veld, A. Kohlmeyer, S. G. Moore, T. D. Nguyen, R. Shan, M. J. Stevens, J. Tranchida, C. Trott, and S. J. Plimpton, LAMMPS a flexible simulation tool for particle-based materials modeling at the atomic, meso, and continuum scales, Computer Physics Communications 271, 108171 (2022).
- [29] G. Henkelman, B. P. Uberuaga, and H. Jónsson, A climbing image nudged elastic band method for finding saddle points and minimum energy paths, The Journal of Chemical Physics 113, 9901 (2000).
- [30] J. Byggmästar, tabgap GitLab (2025).
- [31] A. Ramasubramaniam, Interatomic potentials for hydrogen in α-iron based on density functional theory,

- Physical Review B **79**, 10.1103/PhysRevB.79.174101 (2009).
- [32] M. Wen, A new interatomic potential describing Fe-H and H-H interactions in bcc iron, Computational Materials Science 197, 110640 (2021).
- [33] F.-S. Meng, J.-P. Du, S. Shinzato, H. Mori, P. Yu, K. Matsubara, N. Ishikawa, and S. Ogata, General-purpose neural network interatomic potential for the α -iron and hydrogen binary system: Toward atomic-scale understanding of hydrogen embrittlement, Physical Review Materials **5**, 113606 (2021).
- [34] Y. Tateyama and T. Ohno, Stability and clusterization of hydrogen-vacancy complexes in alpha-Fe: An ab initio study, Physical Review B 67, 174105 (2003).
- [35] D. E. Jiang and E. A. Carter, Diffusion of interstitial hydrogen into and through bcc Fe from first principles, Physical Review B 70, 064102 (2004).
- [36] A. Boda, S. M. Ali, K. T. Shenoy, and S. Mohan, Adsorption, Absorption, Diffusion, and Permeation of Hydrogen and Its Isotopes in bcc Bulk Fe and Fe(100) Surface: Plane Wave-Based Density Functional Theoretical Investigations, The Journal of Physical Chemistry C 123, 23951 (2019).
- [37] Q. Chen, Q. Yao, Y.-L. Liu, Q.-F. Han, and F. Ding, Temperature-dependent dissolution and diffusion of H isotopes in iron for nuclear energy applications: First-principles and vibration spectrum predictions, International Journal of Hydrogen Energy 42, 11560 (2017).
- [38] K. Hirata, S. Iikubo, M. Koyama, K. Tsuzaki, and H. Ohtani, First-Principles Study on Hydrogen Diffusivity in BCC, FCC, and HCP Iron, Metallurgical and Materials Transactions A 49, 5015 (2018).
- [39] M. Nagumo, Hydrogen related failure of steels a new aspect. Materials Science and Technology 20, 940 (2004).
- [40] H. Momida, Y. Asari, Y. Nakamura, Y. Tateyama, and T. Ohno, Hydrogen-enhanced vacancy embrittlement of grain boundaries in iron, Physical Review B 88, 144107 (2013).
- [41] M. Itakura, H. Kaburaki, M. Yamaguchi, and T. Okita, The effect of hydrogen atoms on the screw dislocation mobility in bcc iron: A first-principles study, Acta Materialia 61, 6857 (2013).
- [42] Y. Zhao and G. Lu, QM/MM study of dislocation—hydrogen/helium interactions in α-Fe, Modelling and Simulation in Materials Science and Engineering 19, 065004 (2011).
- [43] S. Starikov, D. Smirnova, T. Pradhan, Y. Lysogorskiy, H. Chapman, M. Mrovec, and R. Drautz, Angulardependent interatomic potential for large-scale atomistic simulation of iron: Development and comprehensive comparison with existing interatomic models, Physical Review Materials 5, 063607 (2021).
- [44] G. Lv, M. Zhang, H. Zhang, and Y. Su, Hydrogen diffusion and vacancy clusterization in iron, International Journal of Hydrogen Energy 43, 15378 (2018).
- [45] Y. Zhu, Z. Li, and M. Huang, Solute hydrogen effects on plastic deformation mechanisms of α -Fe with twist grain boundary, International Journal of Hydrogen Energy 43, 10481 (2018).
- [46] J. Wang, P. Du, X. Jia, and Y. Zhang, Molecular dynamics study on the effect of hydrogen on the plastic behavior of α-Fe crack tip, Materials Today Communications 39, 109292 (2024).

- [47] K. Kiuchi and R. B. McLellan, The solubility and diffusivity of hydrogen in well-annealed and deformed iron, Acta Metallurgica 31, 961 (1983).
- [48] H. Matsui, H. Kimura, and S. Moriya, The effect of hydrogen on the mechanical properties of high purity iron I. Softening and hardening of high purity iron by hydrogen charging during tensile deformation, Materials Science and Engineering 40, 207 (1979).
- [49] T. Hiroi, Y. Fukai, and K. Mori, The phase diagram and superabundant vacancy formation in Fe-H alloys revisited, Journal of Alloys and Compounds Proceedings of the 9th International Symposium on Metal-Hydrogen Systems, Fundamentals and Applications (MH2004), 404-406, 252 (2005).
- [50] J. V. Badding, R. J. Hemley, and H. K. Mao, High-Pressure Chemistry of Hydrogen in Metals: In Situ Study of Iron Hydride, Science 253, 421 (1991).
- [51] Y. Fukai, A. Fukizawa, K. Watanabe, and M. Amano, Hydrogen in Iron–Its Enhanced Dissolution under Pressure and Stabilization of the γ Phase, Japanese Journal of Applied Physics 21, L318 (1982).
- [52] D. Psiachos, T. Hammerschmidt, and R. Drautz, Ab initio study of the modification of elastic properties of α -iron by hydrostatic strain and by hydrogen interstitials, Acta Materialia **59**, 4255 (2011).
- [53] J. J. Adams, D. S. Agosta, R. G. Leisure, and H. Ledbetter, Elastic constants of monocrystal iron from 3 to 500 K, Journal of Applied Physics 100, 113530 (2006).
- [54] E. Lunarska, A. Zielinski, and M. Smialowski, Effect of hydrogen on shear modulus of polycrystalline α iron, Acta Metallurgica 25, 305 (1977).
- [55] A. Stukowski and K. Albe, Extracting dislocations and non-dislocation crystal defects from atomistic simulation data, Modelling and Simulation in Materials Science and Engineering 18, 085001 (2010).
- [56] A. Stukowski, Visualization and analysis of atomistic simulation data with OVITO-the Open Visualization Tool, Modelling and Simulation in Materials Science and Engineering 18, 015012 (2009).
- [57] A. Stukowski, V. V. Bulatov, and A. Arsenlis, Automated identification and indexing of dislocations in crystal interfaces, Modelling and Simulation in Materials Science and Engineering 20, 085007 (2012).
- [58] D. Kandaskalov, C. Mijoule, and D. Connétable, Study of multivacancies in alpha Fe, Journal of Nuclear Materials 441, 168 (2013).
- [59] A. Barnoush and H. Vehoff, Recent developments in the study of hydrogen embrittlement: Hydrogen effect on dislocation nucleation, Acta Materialia 58, 5274 (2010).
- [60] H. Vehoff and W. Rothe, Gaseous hydrogen embrittlement in FeSi- and Ni-single crystals, Acta Metallurgica 31, 1781 (1983).
- [61] H. Vehoff and H. K. Klameth, Hydrogen embrittlement and trapping at crack tips in Ni-single crystals, Acta Metallurgica 33, 955 (1985).
- [62] J. Li, Z. Wu, P. Yin, L. Teng, C. Zhang, G. Deng, Y. Luo, and L. Jiang, Temperature-dependent hydrogeninduced crack propagation behaviour and mechanism in polycrystalline α-iron: Insights from molecular dynamics simulations, International Journal of Hydrogen Energy 85, 500 (2024).
- [63] M. Tanaka, E. Tarleton, and S. G. Roberts, The brittle–ductile transition in single-crystal iron, Acta

- Materialia 56, 5123 (2008).
- [64] Z. Wang, X. Shi, X.-S. Yang, W. He, S.-Q. Shi, and X. Ma, Atomistic simulation of the effect of the dissolution and adsorption of hydrogen atoms on the fracture of α-Fe single crystal under tensile load, International Journal of Hydrogen Energy 46, 1347 (2021).
- [65] V. A. Borodin and P. V. Vladimirov, Molecular dynamics simulations of quasi-brittle crack development in iron, Journal of Nuclear Materials Proceedings of the International DEMETRA Workshop on Development and Assessment of Structural Materials and Heavy Liquid Metal Technologies for Transmutation Systems, 415, 320 (2011).
- [66] J. J. Möller, M. Mrovec, I. Bleskov, J. Neugebauer, T. Hammerschmidt, R. Drautz, C. Elsässer, T. Hickel, and E. Bitzek, \${110}\$ planar faults in strained bcc

- metals: Origins and implications of a commonly observed artifact of classical potentials, Physical Review Materials 2, 093606 (2018), publisher: American Physical Society.
- [67] K. Sakaki, T. Kawase, M. Hirato, M. Mizuno, H. Araki, Y. Shirai, and M. Nagumo, The effect of hydrogen on vacancy generation in iron by plastic deformation, Scripta Materialia 55, 1031 (2006).
- [68] S. Li, Y. Li, Y.-C. Lo, T. Neeraj, R. Srinivasan, X. Ding, J. Sun, L. Qi, P. Gumbsch, and J. Li, The interaction of dislocations and hydrogen-vacancy complexes and its importance for deformation-induced proto nano-voids formation in α-Fe, International Journal of Plasticity 74, 175 (2015).
- [69] L. Feng, W. Tang, Z. Chen, X. Zhang, Y.-W. Zhang, W. Li, M. Xiang, and X. Yao, Atomistic insights into hydrogen-enhanced strain-induced vacancy in α iron across varied strain rates, Scripta Materialia **252**, 116246 (2024).